MULTIPHYSICS FINITE ELEMENT ANALYSIS OF IN-PILE SENSORS FOR ADVANCED NUCLEAR REACTORS

by
Takoda Linn Bingham

A thesis

submitted in partial fulfillment

of the requirements for the degree of

Master of Science in Mechanical Engineering

Boise State University

August 2020

BOISE STATE UNIVERSITY GRADUATE COLLEGE

DEFENSE COMMITTEE AND FINAL READING APPROVALS

of the thesis submitted by

Takoda Linn Bingham

Thesis Title: Multiphysics Finite Element Analysis of In-pile Sensors for Advanced Nuclear Reactors

Date of Final Oral Examination: 10 July 2020

The following individuals read and discussed the thesis submitted by student Takoda Linn Bingham, and they evaluated their presentation and response to questions during the final oral examination. They found that the student passed the final oral examination.

Zhangxian Deng, Ph.D.	Chair, Supervisory Committee
Dylan Mikesell, Ph.D.	Member, Supervisory Committee
Mahmood Mamivand, Ph.D.	Member, Supervisory Committee

The final reading approval of the thesis was granted by Zhangxian Deng, Ph.D., Chair of the Supervisory Committee. The thesis was approved by the Graduate College.

DEDICATION

I would like to dedicate this to my family, especially my parents Tim and Tammy Bingham, for their unrelenting support of my goals in education and in life. They taught me my values and dedication that has kept me pushing for the best. I would also like to dedicate this to my beautiful fiancé Carly Becker, who has constantly supported me and made sure I was taking care of myself through this whole process. To my brother Jacob Bingham and sister in law Amanda Bingham, for the hours they spent combing over all my bad grammar, run on sentences, and vague information. I would also like to dedicate this to my friend Bradley Henderson, who spent many late nights studying with me in both undergrad and graduate school.

ACKNOWLEDGMENTS

Special thanks to my lab members and my advisor Dr. Zhangxian Deng. Dr. Deng's guidance, feedback, and mentorship was instrumental in progressing my thesis, models, and technical writing. The support of Dr. Mahmood Mamivand in the classroom, as an undergraduate researcher, and in the application process for the accelerated master's program allowed for academic success further than I expected when I started at Boise State. Even though I did not end up in his lab, he has continued to support me as a part of my committee. Dr. David Estrada and Dr. Brian Jaques group provided sensors and data that helped with experimental testing and FEA analysis. Nick McKibben provided the manufactured lithium niobate sensor and providing key knowledge into the material science of the sensor. Our work together was a great collaboration and I hope the person who takes over for me has the same working relationship. Thanks to Dr. Dylan Mikesell and Tom O. who trained me on the vibrometer and helped with analyzing the data. This training and data was an important piece needed for FEA modeling. A big thanks to the INL and Dr. Joshua Daw for providing us with information needed to progress each of the sensors.

ABSTRACT

Nuclear reactors have large needs for in-pile sensors that are durable in high temperature, radioactive, and corrosive environments. With the use of multiphysics finite element analysis (FEA) researchers can speed up sensor prototyping. FEA also allows for a better fundamental understanding of sensors and enables sensor optimization. This research focuses on three types of in-pile sensors developed at Idaho National Laboratory: acoustic sensors, linear variable differential transformers (LVDT), and capacitance based strain gauges (CSG). Two acoustic sensors, magnetostrictive waveguides and piezoelectric surface acoustic wave (SAW) sensors were first modeled. These models showed the acoustic wave patterns and estimated the speed of sound. The modeling results were compared to results from laser Doppler vibrometer testing. The model was implemented to enhance the performance of the sensor designs. This research then modeled a LVDT sensor used to measure fuel rod deformation and structural health monitoring. A parametric FEA study was completed for the purpose of sensor miniaturization. The FEA model was also used to investigate the potential of adding a fiber optic cable through the LVDT core. This research eventually modeled CSGs used in nondestructive structural health monitoring. Multiphysics models were used to investigate the discrepancies in experiments and previous analytical models.

TABLE OF CONTENTS

DEDICATION iv

ACKNOWLEDGMENTS v

ABSTRACT vi

LIST OF TABLES ix

LIST OF FIGURES x

LIST OF ABBREVIATIONS xiii

CHAPTER ONE: INTRODUCTION 1

CHAPTER TWO: PIEZOELECTRIC ULTRASONIC THERMOMETER 5

2.1 Introduction 5

2.2 Methods 7

2.2.1 Vibrometer Testing 7

2.2.2 Finite Element Analysis 9

2.3 Results and Discussion 14

2.3.1 Vibrometer Testing 14

2.3.2 Finite Element Analysis 16

2.4 Conclusion 21

2.4.1 Vibrometer Testing 21

2.4.2 Finite Element Analysis 23

CHAPTER THREE: MAGNETOSTRICTIVE ULTRASONIC THERMOMETER 25

3.1 Introduction....25
3.2 Methods....27
3.2.1 Testing....27
3.2.2 Finite Element Analysis....29
3.3 Results and Discussion....30
3.3.1 Testing....30
3.3.2 Finite Element Analysis....34
3.4 Conclusion....37
CHAPTER FOUR: CAPACITANCE BASED STRAIN GUAGE....39
4.1 Introduction....39
4.2 Methods....41
4.3 Results and Discussion....42
4.4 Conclusion....43
CHAPTER FIVE: LINEAR VARIABLE DIFFERENTIAL TRANSFORMER....44
5.1 Introduction....44
5.2 Methods....46
5.3 Results and Discussion....48
5.4 Conclusion....50
CHAPTER SIX: CONCLUSIONS....51
REFERENCES....53

LIST OF TABLES

Table 1 Material properties of PZT-5A used during simulation..... 12

Table 2 Reflection amplitudes and times for each location for galfenol waveguide. 32

Table 3 Calculated time of flight for galfenol waveguide between different reflections and locations. 32

Table 4 Voltage amplitude and time data for reflection locations from COMSOL simulation..... 36

Table 5 Calculated time of flight for galfenol waveguide between different reflections and locations from COMSOL simulation. 37

Table 6 Key material properties used in the physics of the COMSOL model..... 42

LIST OF FIGURES

Figure 1 Example of the piezoelectric effect (left) and the converse piezoelectric effect (right). The dotted outlined material is the original material with no outside boundary conditions. The solid grey material is the material response after either strain or voltage is applied. 5

Figure 2 Dimensions of the Lithium Niobate SAW sensor (left) and the actual printed sensor (right). All dimensions are in mm. 8

Figure 3 Vibrometer testing setup for the piezoelectric sensor with attached electrode leads. 9

Figure 4 Model geometry and boundary conditions. 10

Figure 5 Voltage over time for excitation electrodes. 11

Figure 6 Longitudinal mode SAW sensor geometry and constraints. 13

Figure 7 Excitation voltage for longitudinal-mode piezoelectric sensor. 14

Figure 8 Vibration amplitude (color scale) over time along the scanning field on the lithium niobate substrate. The red line shows the p-wave. 15

Figure 9 Voltage data from sensing electrode leads during testing. The red line shows the time of arrival of the p-wave. 16

Figure 10 Stress and deformation in the piezoelectric substrate with silver interdigital electrodes after the excitation voltage ends. P-wave is shown by the green line and s-wave is shown by the green circle. Deformation is increased by 8E5 times for visual purposes. 17

Figure 11 The excitation voltage (top) and the sensing voltage (bottom) for interdigital electrode on PZT-5A piezoelectric substrate. The time of arrival for the p-wave is shown as a red line. 18

Figure 12 The x-direction stress and x-y deformation in the substrate immediately after the end of the voltage excitation. The deformation is increased by 7E6 times for visual purposes. 18

Figure 13 Comparison of the excitation voltage (top) and the sensing voltage (bottom) for the longitudinal-mode piezoelectric sensor. The time of arrival of the p-wave is shown as a red line. 19

Figure 14 The x-direction stress and x-y deformation in the substrate with shifted electrodes when the acoustic wave starts to reflect off the fixed end. The deformation is increased by 7E6 times for visual purposes. 20

Figure 15 Comparison x-direction stress and x-y deformation in the substrate immediately after the end of the Gaussian pulse voltage excitation (top). And a short time after the excitation ends and stress is released (bottom). The deformation is increased by 7E6 times for visual purposes. 21

Figure 16 Possible wave propagation direction and the scanning field in lithium niobate substrate 22

Figure 17 Magnetostrictive material before and after magnetic field is applied. 25

Figure 18 Dimensions and geometry of the cross section view of the magnetostrictive transducer and waveguide. The full sensor is revolved around center axis shown. 27

Figure 19 Square wave with amplitude (A) and pulse width (W). Example of impulse voltage used for experiments pictured right. 28

Figure 20 Nickel wire vibrometer experimental setup (left) and the scanning field used in testing (right). 29

Figure 21 2-D axisymmetric model of galfenol waveguide sensor in COMSOL. 30

Figure 22 Voltage comparison of 0 dB and 20 dB for DC current of 2 A and voltage Amplitude of 100 V. 31

Figure 23 A typical waveform of reflection voltage. 31

Figure 24 Vibration amplitude (color scale) over time along the scanning field of the nickel wire. Green line is the p-wave and the blue line is the s-wave. 33

Figure 25 Magnetic flux density distribution when a current of 2.0 A is applied to the DC coil. 34

Figure 26 AC coil input current found using simulation 35

Figure 27 Comparison of simulated and measured voltage reflections. 36

Figure 28 Diagram of CSG layout and design that is similar to the manufactured and tested sensor. Dimension variables shown are used in the capacitance equations (6) and (7). 39

Figure 29 Capacitive sensor model geometry and boundary conditions..... 41

Figure 30 Maxwell capacitance and relative change in capacitance with increase in strain..... 42

Figure 31 Gauge factor for changing electrode height and width. 43

Figure 32 General LVDT component diagram. 44

Figure 33 Equation and basic operation diagram of LVDT sensor..... 45

Figure 34 LVDT characterization data measured at the INL. 46

Figure 35 2-D axisymmetric model of the LVDT sensor. 47

Figure 36 Nonlinear HB curve for LVDT core. 48

Figure 37 Voltage output of LVDT relative to the core position for frequency-domain..... 49

Figure 38 Sensitivity for an added thru hole in the core of the LVDT sensor. 50

LIST OF ABBREVIATIONS

ANML	Advanced Nanomaterials and Manufacturing Laboratory
AWG	American Wire Gauge
CSG	Capacitance based Strain Gauge
EM	Electro-Magnetic
FEA	Finite Element Analysis
INL	Idaho National Laboratory
LVDT	Linear Variable Differential Transformer
NASA	National Aeronautics and Space Administration
P-wave	Pressure Wave
SAW	Surface Acoustic Wave
S-wave	Shear Wave
U.S.	United States

CHAPTER ONE: INTRODUCTION

Currently in the U.S., 74 of the 100 operational reactors have been granted a 20 year expansion on the original 40 year license [1]. To extend the life of the operation past 2050 they would need extension past 60 years [1]. During 2013 alone an estimated 6.4 billion dollars in capital went to maintenance and upgrades [1]. There is also a need for new technology to be implemented into new types of reactors. The molten chloride fast reactor needs new sensors to tackle the wide variety of needs and safety concerns. There is a need for extra safety and higher efficiency as the life of the current reactor increases and new reactors are developed. The INL has been developing sensors to tackle some of the needs that these reactors have.

Acoustic sensors are being evaluated at the INL as ultrasonic thermometers. There are two types of acoustic sensors being tested for temperature sensing: magnetostrictive waveguides and piezoelectric surface acoustic wave (SAW) sensors. These devices work by relating the speed of sound to a known temperature of the material using an equation. Ultrasonic thermometers can be used for getting live and continuous temperature data from inside the nuclear reactors. Temperature sensors that are currently being used are melt wires and thermocouples. Melt wires are limited to discrete data points and are measured post-irradiation. Thermocouples are also limited by certain temperature ranges and can become decalibrated in high temperatures and radioactive environments [2]. Any temperature device that uses electrical measurements is limited by the electrical signal, as the temperatures exceed 1800°C the electrical insulators degrade and cause electric

shunting errors [2]. Ultrasonic thermometers can use waveguides to protect the electrical components of the sensor from large temperatures. With the electrical components protected the ultrasonic thermometers are only limited by the material melting point, which can provide temperature readings above double the temperature that electrical thermometers can produce. Oak Ridge National Laboratory has verified the capability of determining the temperature using a frequency analysis of a SAW sensor. The device was only capable of a temperature resolution of 2.36% [3]. When the INL tested their current sensors with a time domain analysis they were able to get slightly better resolution of between 1-2% [2]. To improve the resolution of these devices and guide sensor development, multiphysics FEA was used to model both the piezoelectric and magnetostrictive temperature sensors. The models created for this thesis will be used as the base for more accurate models once materials properties have been experimentally found. Experiments using a laser Doppler vibrometer and ultrasonic transducer were developed and presented for future researchers. These experiments will be used to help determine material properties and validate model accuracy. Along with temperature sensing the INL has the need to measure displacements of materials during irradiation.

LVDT sensors are well developed, simple sensors that measure linear displacement. The LVDT works by measuring the voltage in two coils that is caused by the magnetic field around a magnetic core. The difference in voltage between the two coils is then related to the displacement. The sensitivity of the device is limited only by the noise present in the system. The displacement sensors are versatile and are used as the base sensors in several different types of devices. The INL designed and used LVDT sensors for creep testing for new material that are planned to be used in high temperature

radiation [4]. The LVDT allows for the data from tests to be analyzed without the need of specimen removal. The irradiation tests can be ran until the desired effect is reached rather than removing and returning the test piece. [4]. Other labs are also using the LVDT for nuclear analysis. The Institute for Energy Technology is using the LVDT for the Halden Reactor Project as the base sensor for pressure transducers, fuel centerline temperatures, cladding elongation, and fuel elongation [5]. The fast analysis of new materials during irradiation allows for better cladding and fuels to be tested in shorter amounts of time. The current LVDT devices on the market are larger than what is desired by the INL and only withstands lower temperatures. Multiphysics FEA was used to develop a model of the current LVDT device. Once this model is accurate and reliable the simulation can be used to help develop a miniaturized LVDT sensor. Later in the thesis model and verification data is presented. This thesis also goes over the impact of putting a thru-hole in the LVDT core. The hole would be used as a port for a fiber optic cable. Adding a port along with the LVDT sensor will reduce the use of a different slot for a fiber optic cable in the reactor. The freed up slot can then be used for other devices or sensors. FEA was used to determine the impact without actually damaging the LVDT. The INL is doing research on many devices with applications in the nuclear field and outside it.

The INL in conjunction with NASA has been developing small flexible CSG sensors to provide non-destructive structural health monitoring. Soft structural materials like Kevlar parachute chord have needs for this type of monitoring. Flexible CSG sensors have been developed to allow for monitoring of strain in these types of materials [6]. These sensors were created using a typical interdigital electrode designs. The electrode

designs were then applied to a flexible polymer substrate [6]. The device works by measuring the decrease in capacitance and relates it back to strain. The capacitance decreases due to the increase in spacing of the interdigital electrode pairs. Current commercial devices consist of parallel plates rather than the interdigital electrodes. The parallel plate design is bulky and limited to strain measurements perpendicular to the sensor [6]. Another device that measures strain is the resistance based strain gauge. CSG have higher gauge factors than resistance based strain gauges. Resistance based strain gauges have resistivity hysteresis which limits performance [6]. The CSG's do not have the limitations with resistivity and can provide higher performance [6]. Analytical models were used to try and verify experimental results. The analytical equations underestimated the capacitance. The use of FEA was used to try and explain the discrepancies with the analytical model and the experimental data. The model was also used for a parametric study to determine the impact of electrode size. The impact was measured by the change in gauge factor as the electrode height and width changed. The following chapters go over the testing, FEA modelling, and conclusions for all of the different sensors.

CHAPTER TWO: PIEZOELECTRIC ULTRASONIC THERMOMETER

2.1 Introduction

Piezoelectric materials are used in many applications and are useful because of their ability to convert energy. This material can convert between electric potential and stress (either bending, compression, tension, or torsion).

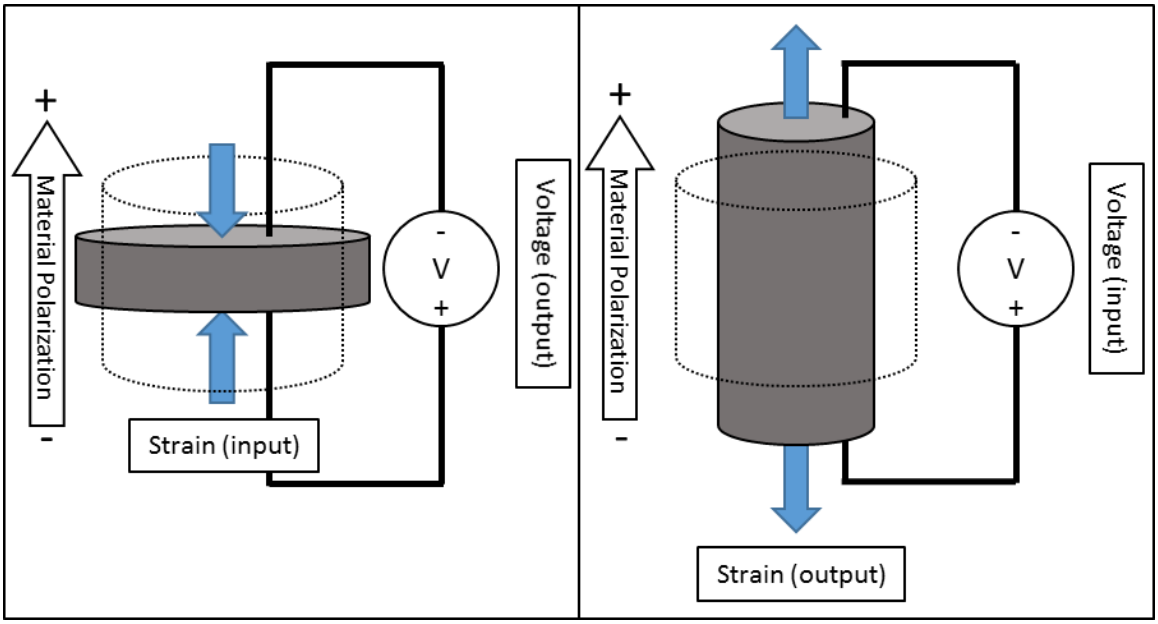

Figure 1 Example of the piezoelectric effect (left) and the converse piezoelectric effect (right). The dotted outlined material is the original material with no outside boundary conditions. The solid grey material is the material response after either strain or voltage is applied.

Piezoelectric solids have a linear relationship between electric polarization and stress [7]. The linear relationship can be expressed as:

$$P_i = \sum_{j,k} d_{ijk}\sigma_{jk}, \qquad (1)$$

where P is the induced polarization, d is the piezoelectric tensor, and σ is the stress tensor [7]. The relationship is what allows for the material to be used as a sensor. As the material is under stress it induces a polarization that causes an electric potential. For actuation the converse piezoelectric relationship is used. The converse piezoelectric effect is when a strain or shape change is caused from an applied electric field [7]. The converse relationship is also a linear relationship.

$$S_{jk} = \sum_i d_{ijk} E_i, \qquad (2)$$

where S is the strain tensor and E is the electric field [7]. A basic example of the piezoelectric effect and the converse piezoelectric effect is shown in Figure 1. In practice, piezoelectric materials allow for both actuation and sensing through electrical leads attached to the material surface.

Using the actuation, a piezoelectric material can be used to produce an ultrasonic wave like that needed for ultrasonic thermometry. An ultrasonic thermometer is one method of sensing temperature. It works by using the relationship between the speed of sound in a material and its Young's modulus. As the temperature of the sensor increases, the Young's modulus of the material decreases, and the speed of sound increases. The speed of sound through the material can be calculated using the time of flight of the wave and the distance travelled. Then from the previous relationship the speed can be used to retrieve the temperature. These thermometers can be made by attaching conductive electrodes to the surface of a piezoelectric substrate and exciting mechanical waves in the material and sensing the reflections produced.

Using piezoelectric materials for an ultrasonic thermometer have many benefits. The first benefit is its durability in extreme temperatures and radioactive environments,

like those found in nuclear reactors. The sensors can also be made at a low cost and with a smaller footprint using additive manufacturing. Sensor footprint is important because nuclear reactors have limited space. The ultrasonic method also allows for real time data on temperatures, along with rapid detection of critical fault conditions.

Multiphysics finite element analysis is needed to model this material to speed up sensor prototyping, and better understand sensor fundamentals. Multiphysics FEA also allows for solving of complex systems of differential equations. These differential equations allow for solid mechanics, electrodynamics, and the piezoelectric effect to be solved for simultaneously. FEA needs to be tuned using real data to ensure model accuracy. A laser Doppler vibrometer was used to characterize the material and compare results from FEA.

2.2 Methods

2.2.1 Vibrometer Testing

A piezoelectric ultrasonic thermometer was manufactured by printing two pairs of inter-digital silver electrodes on top of a 10 mm by 10 mm by 0.5 mm lithium niobate Y-cut 128° substrate. The sensor in Figure 2 is called a Rayleigh SAW sensor. The sensor was manufactured by Nicholas McKibben in Boise State's ANML.

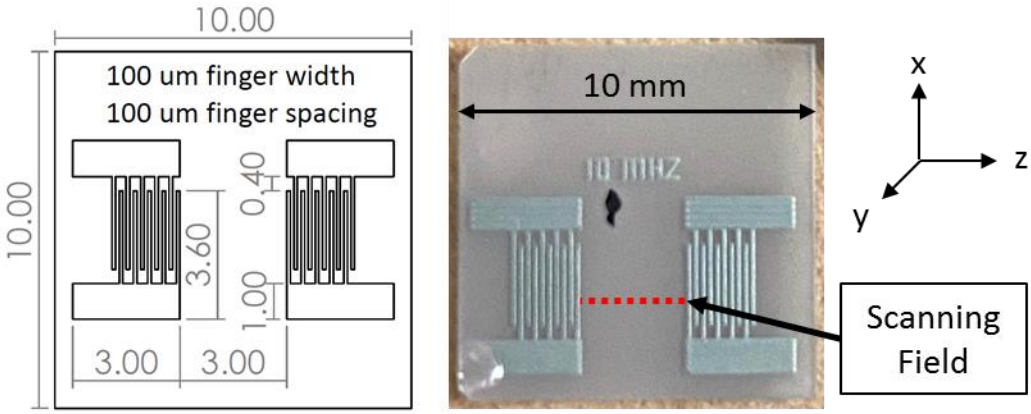

Figure 2 Dimensions of the Lithium Niobate SAW sensor (left) and the actual printed sensor (right). All dimensions are in mm.

The substrate is then placed on a foam support to replicate a free-free boundary condition. The piezoelectric effect is effective in the z-direction of the substrate for Y-cut lithium niobate [7]. The sensor was created in the z-direction, but the correct amplifier was not available. Therefore, an impulse is provided by an Nd:YAG laser on the left edge of the substrate parallel to the z-direction. The out of plane vibration (in the y-direction) on the surface of the substrate is measured along the scanning field, shown in Figure 2, using a Polytec PSV-400 laser doppler vibrometer. The scanning field is 3 mm long and consists of 61 data locations along a straight line. Each measurement point was measured for 25 μs and was stacked 200 times to reduce the measurement noise. The vibrometer has a sampling frequency of 2 MHz and a minimum laser spot size of 36 μm.

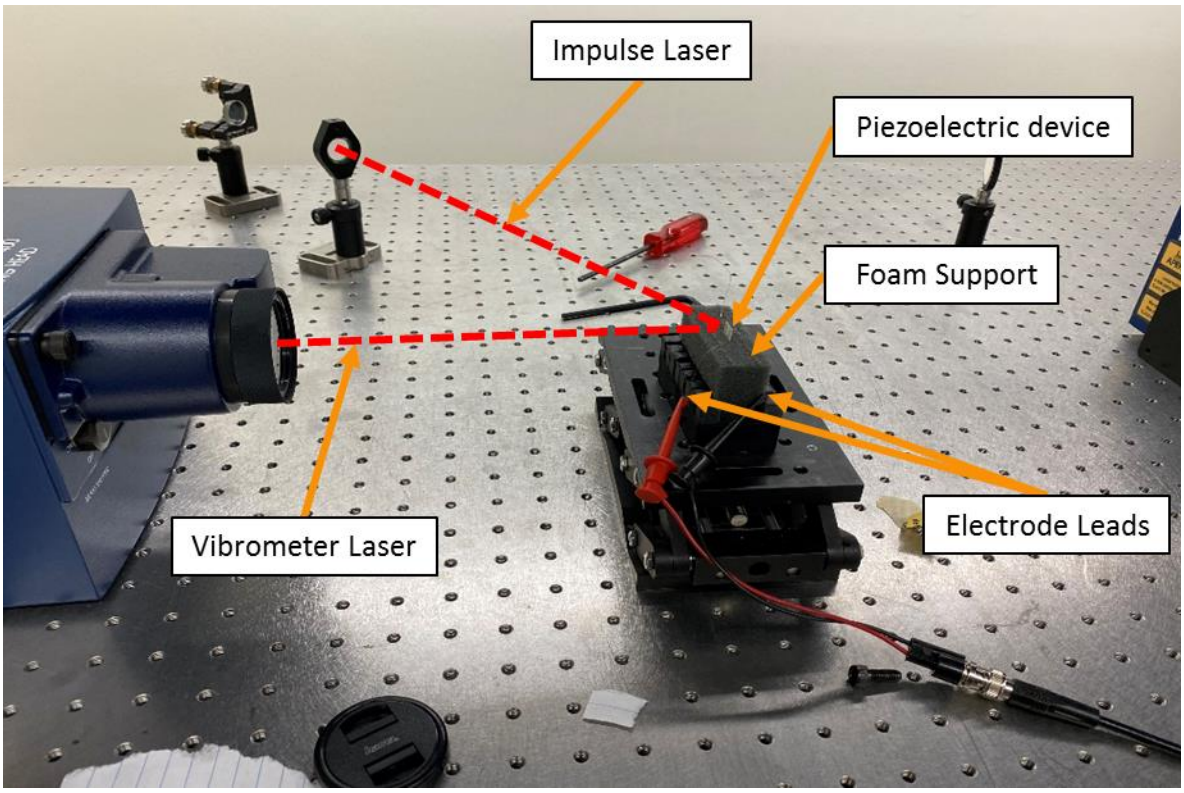

Figure 3 Vibrometer testing setup for the piezoelectric sensor with attached electrode leads.

Figure 3 shows the lithium niobate piezoelectric sensor and the layout of the laser excitation and the vibrometer laser. Electrode leads were attached to the electrode pads farthest away from the source laser to measure voltage from the piezoelectric effect in the lithium niobate.

2.2.2 Finite Element Analysis

2.2.2.1 Rayleigh SAW Sensor

The Rayleigh SAW sensor produces waves that propagate along the top surface of the sensor. The model consists of silver interdigital electrodes on top of a square PZT-5A piezoelectric substrate. The dimensions of the square substrate are 76.2 mm width and 0.6 mm thickness. A 2-D cross sectional representation of the sensor is used to alleviate large data sets and long computation times. A time domain analysis was implemented in order

to capture the transient response of the sensor after excitation. In order to alleviate the bending mode of the substrate during excitation and to allow the acoustic wave to propagate properly, the substrate thickness was increased to 2 mm.

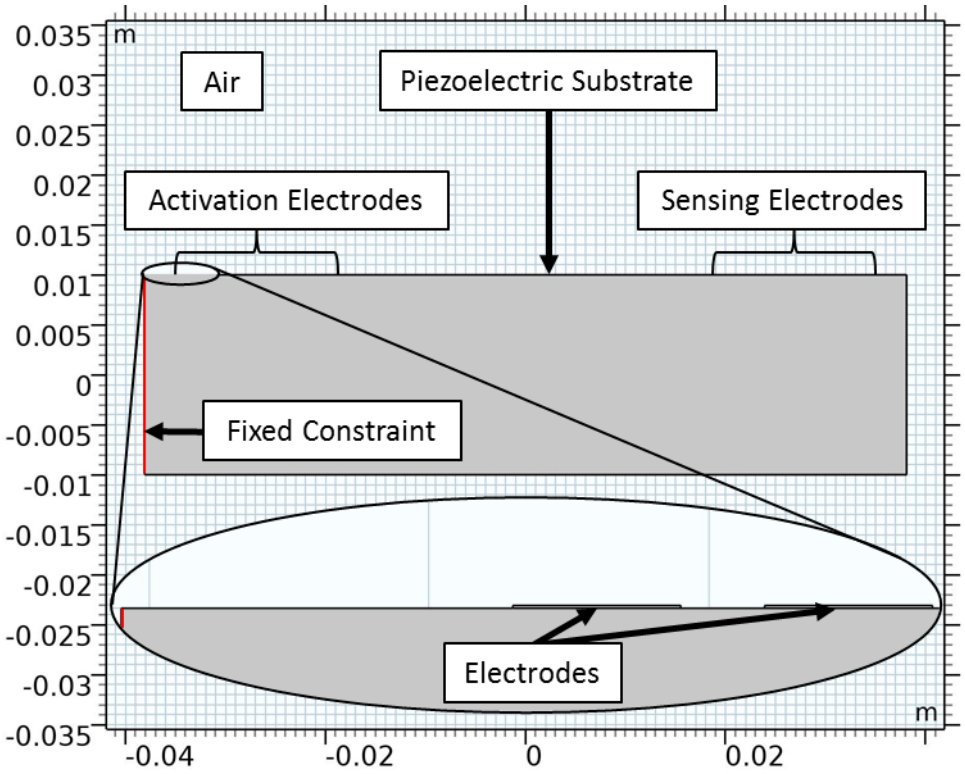

Figure 4 Model geometry and boundary conditions.

Figure 4 shows the 2-D cross sectional view of the model that was constructed in COMSOL Multiphysics. The depth of this model that is in the out of plane direction is 1 mm. A square air domain with a width of 0.23 m is defined to replicate the infinite air around the substrate in practice. The lithium niobate is fixed using a fixed constraint on the left end of the substrate near the activation electrodes. The boundary condition is used to prevent motion and make the substrate act as a cantilever beam with gravity ignored. The silver electrodes have a width of 0.6 mm, height of 2.2 μm, and a spacing of 0.3 mm. The model contains two sets of ten electrodes on either end of the substrate for voltage

excitation and sensing. The distance between the two sets of electrodes is 64.85 mm (measured from the center of each electrode set). The excitation electrodes alternate from ground to an applied voltage.

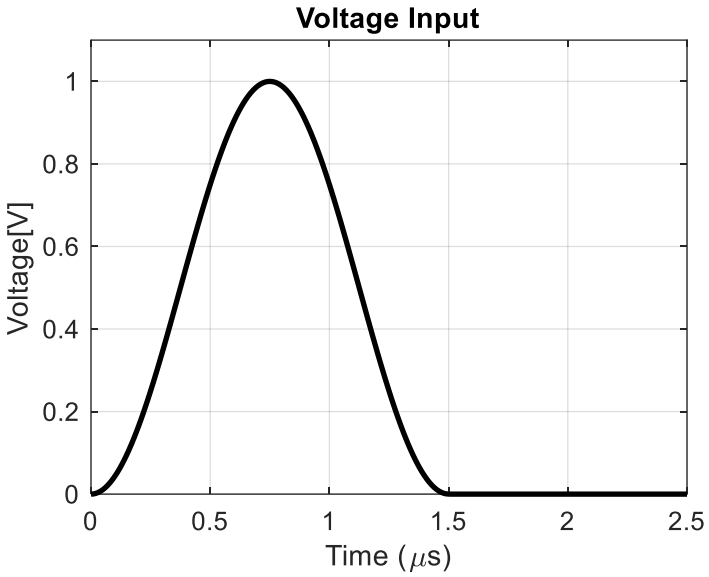

Figure 5 Voltage over time for excitation electrodes.

In Figure 5, the applied voltage is a Gaussian pulse of length 1.5 μs and has an amplitude of 1 V. The material properties that were used in the model are in Table 1 below.

Table 1 Material properties of PZT-5A used during simulation.

Property	Variable	Value	Unit
Density	rho	7750	kg/m^3
Compliance matrix, Voigt notation	{sE11, sE12, sE22, sE13, sE23, sE33, sE14, sE24, sE34, sE44, sE15, sE25, sE35, sE45, sE55, sE16, sE26, sE36, sE46, sE56, sE66} ; sEij = sEji	{1.64e-11, -5.74e-12, 1.64e-11, -7.22e-12, -7.22e-12, 1.88e-11, 0, 0, 0, 4.75e-11, 0, 0, 0, 0, 4.75e-11, 0, 0, 0, 0, 0, 4.43e-11}	1/Pa
Coupling matrix, Voigt notation	{dET11, dET21, dET31, dET12, dET22, dET32, dET13, dET23, dET33, dET14, dET24, dET34, dET15, dET25, dET35, dET16, dET26, dET36}	{0, 0, -1.71e-10, 0, 0, -1.71e-10, 0, 0, 3.74e-10, 0, 5.84e-10, 0, 5.84e-10, 0, 0, 0, 0, 0}	C/N
Relative permittivity	{epsilonrT11, epsilonrT22, epsilonrT33} ; epsilonrTij = 0, when i≠j	{1730, 1730, 1700}	1

2.2.2.2 Longitudinal-mode Sensor

The longitudinal-mode sensor does not produce SAWs, but produces a p-wave instead. For the Longitudinal mode sensor, the material properties listed in Table 1 were used. Again, a 2-D and time domain analysis was used in to analyze the transient response quickly and efficiently. The dimensions used in the model were a substrate thickness of 0.6 mm and width of 76.2 mm. The model geometry and constraints are shown below in Figure 6.

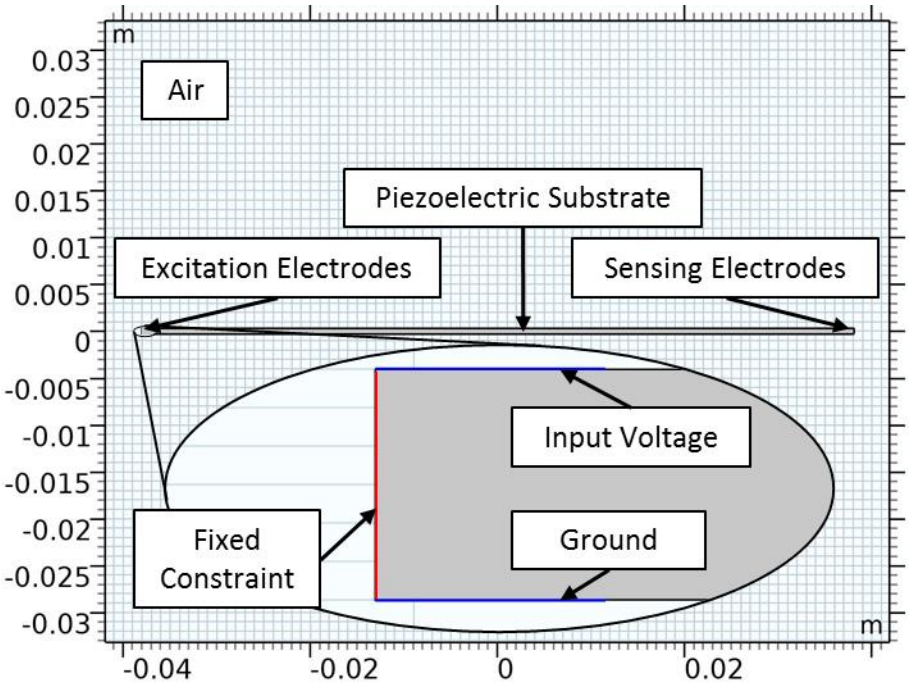

Figure 6 Longitudinal mode SAW sensor geometry and constraints.

The longitudinal mode SAW sensor shown consists of two pairs of electrodes on both ends of the substrate. One pair of electrodes is for excitation and the other pair is for sensing of the generated waves. The silver electrodes have a width of 0.6 mm and a height of 2.2 μm. The model has a fixed constraint on the substrate end next to the excitation electrodes, this prevents motion and constrains the substrate as a cantilevered beam with gravity ignored. The whole model is surrounded by a square air domain with the width 0.23 m to simulate the infinite air surrounding the sensor in practice. The excitation for the model is a sine pulse.

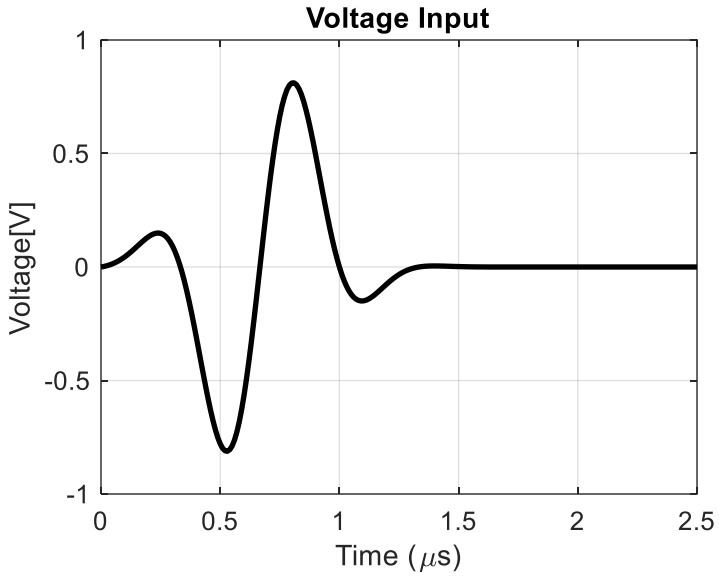

Figure 7 Excitation voltage for longitudinal-mode piezoelectric sensor.

The sine voltage pulse in Figure 7 shows the voltage amplitude of 0.8 V and the pulse length of 1.5 μs.

2.3 Results and Discussion

2.3.1 Vibrometer Testing

The vibrometer records the out of plane sensor vibration along the 3 mm scanning field. This vibration can then be plotted in terms of relative distance from the start of the scanning field and time with the vibration amplitude as the color scale. Then the first arrival of the p-wave can be picked out from the graph.

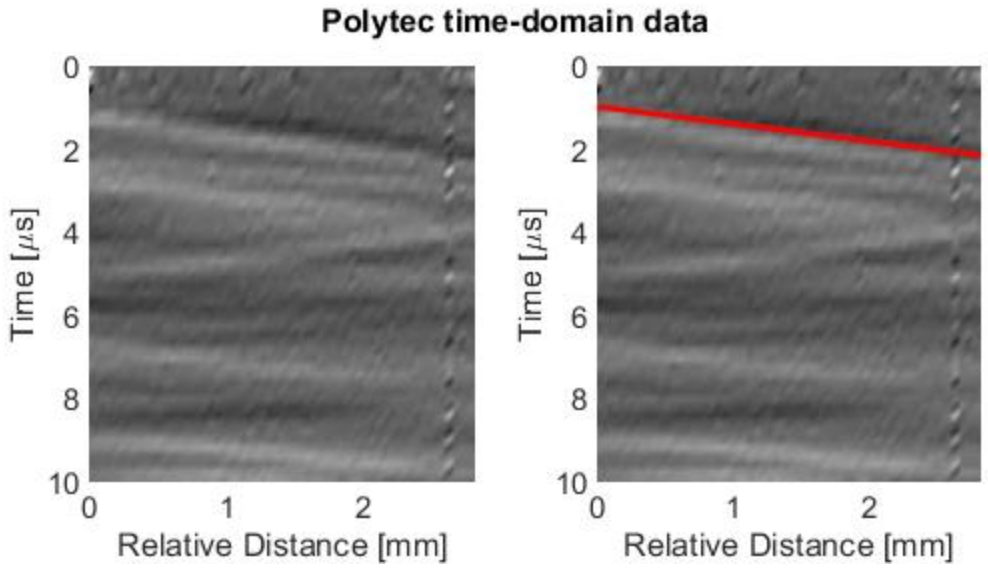

Figure 8 Vibration amplitude (color scale) over time along the scanning field on the lithium niobate substrate. The red line shows the p-wave.

Figure 8 shows the vibration of the lithium niobate along the scanning line, as well as the direct arrival of the p-wave at each scan point. The peaks of the first arrival vibration at each scan point is then found and a wave velocity can be calculated. The pressure, or p-wave velocity, was calculated as 2156.14±157.95 m/s at 95% confidence level. The voltage from the sensing electrode was also collected.

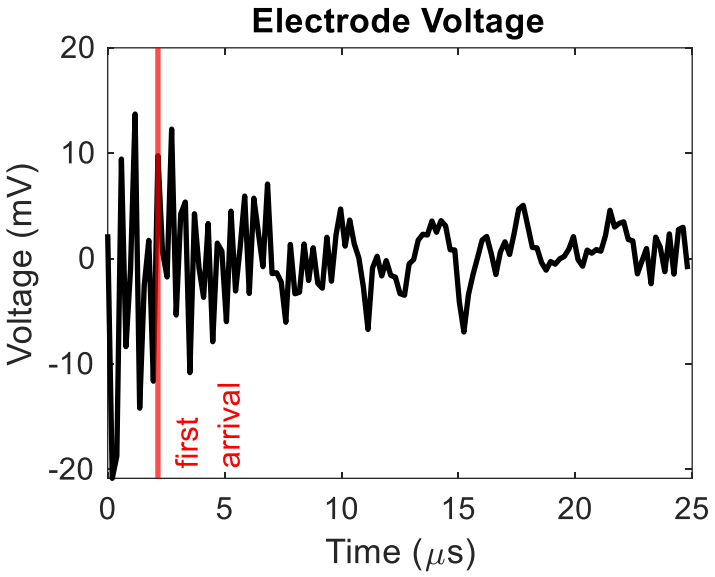

Figure 9 **Voltage data from sensing electrode leads during testing. The red line shows the time of arrival of the p-wave.**

Figure 9 shows the voltage data from the sensing electrodes during the vibration testing. The time of the first arrival is shown as the red line, there is significant signal before the wave even arrives to the electrodes. This is likely electrical interference due to the EM field related to the laser ultrasonic system and could be reduced by using shielded electrodes and connection wires.

2.3.2 Finite Element Analysis

2.3.2.1 Rayleigh SAW Sensor

The FEA simulation was able to produce acoustic waves originating at the center of the excitation electrodes and moving outward in both directions. The stress and deformation in the piezoelectric substrate at 5.5 μs or after the excitation ended is shown in Figure 10.

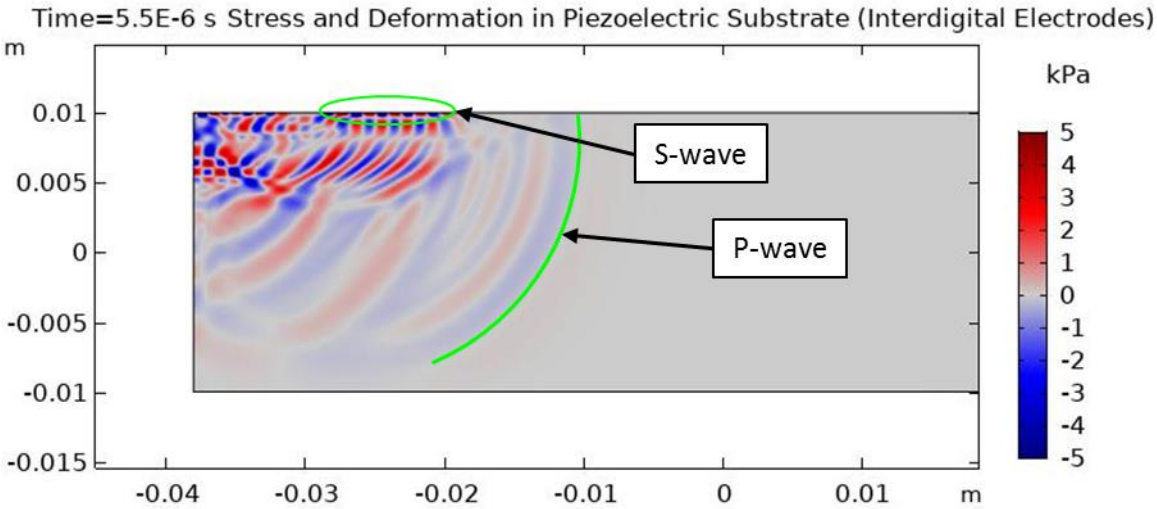

Figure 10 Stress and deformation in the piezoelectric substrate with silver interdigital electrodes after the excitation voltage ends. P-wave is shown by the green line and s-wave is shown by the green circle. Deformation is increased by 8E5 times for visual purposes.

Due to the stress the wave propagates and reaches the sensing electrodes in 31.4 μs. The p-wave is the fastest wave and is shown in Figure 10. The s-waves are slower waves and follow behind the p-wave at the top surface and are circled in Figure 10. However, voltage has been detected on the sensing electrodes long before the surface acoustic wave gets there, as shown in Figure 11.

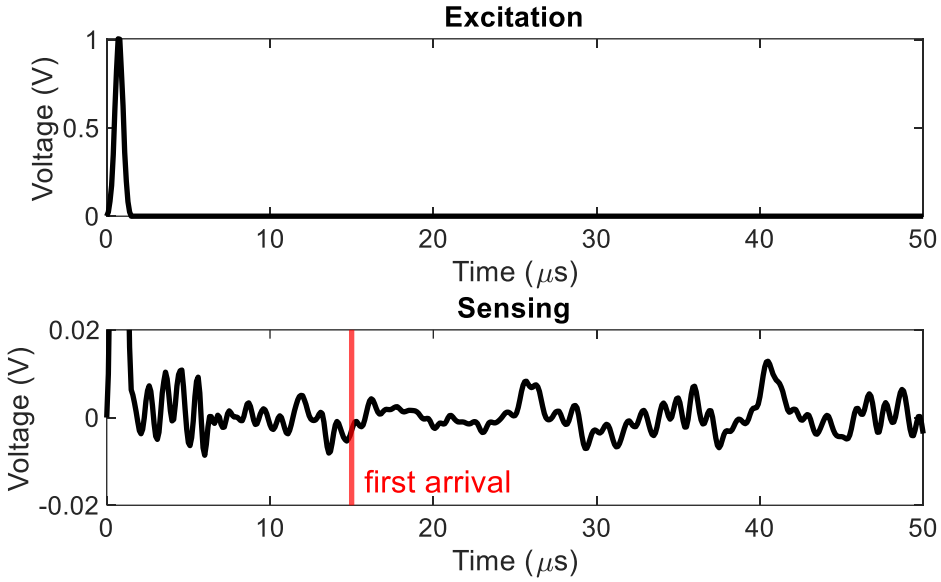

Figure 11 The excitation voltage (top) and the sensing voltage (bottom) for interdigital electrode on PZT-5A piezoelectric substrate. The time of arrival for the p-wave is shown as a red line.

2.3.2.2 Longitudinal-mode SAW Sensor

When the sinusoidal impulse was applied a compressive wave or p-wave formed in the piezoelectric substrate. Since the electrodes were lined up with the edge of the material, the wave propagation was not impacted by any reflections off the fixed end.

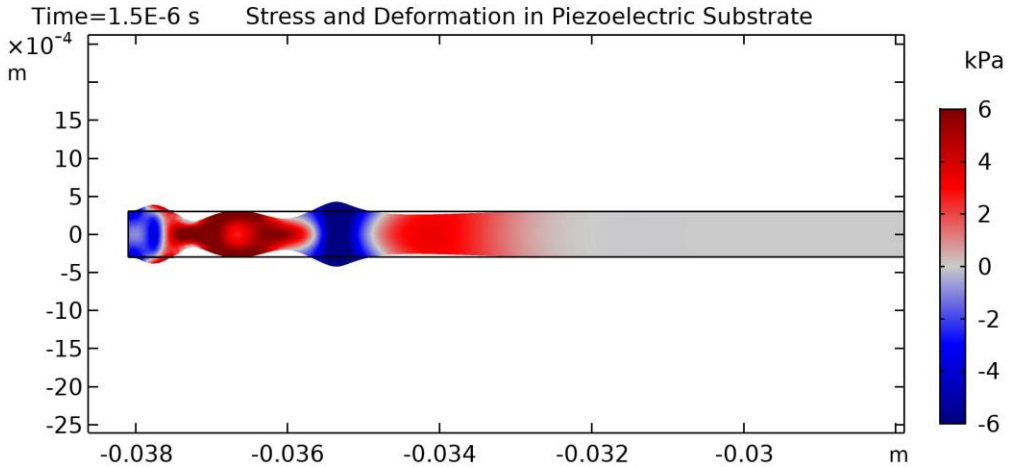

Figure 12 The x-direction stress and x-y deformation in the substrate immediately after the end of the voltage excitation. The deformation is increased by 7E6 times for visual purposes.

Figure 12 shows the stress only in the x-direction after the excitation. This p-wave propagated to the other end of the substrate and started to reflect back. The voltage in the sensing electrodes show a clean arrival of the p-wave created using the longitudinal-mode sensor.

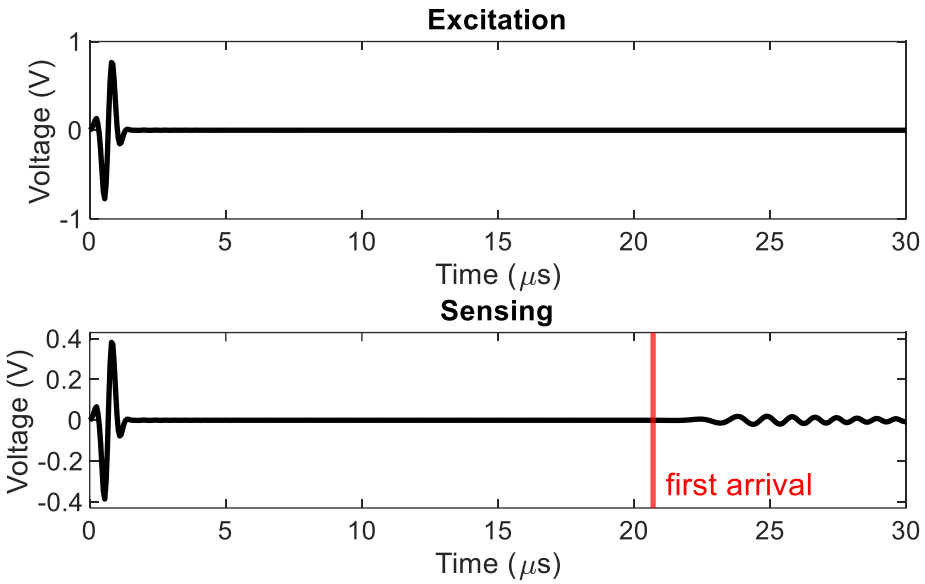

Figure 13 Comparison of the excitation voltage (top) and the sensing voltage (bottom) for the longitudinal-mode piezoelectric sensor. The time of arrival of the p-wave is shown as a red line.

Figure 13 shows the excitation voltage and the sensing voltage. This model shows a time of arrival that is more easily visually interpreted. The excitation reaches the sensing electrode at 20.7 μs. The calculated arrival time for the p-wave is 19.02 μs. The percent difference from the analytical is 8.83%. There was also significant EM interference from the voltage impulse before the p-wave arrived to the sensing electrodes. The model was also altered to see the impact of the placement of the electrode as well as the impact of the voltage impulse. When the excitation electrodes were moved in just 10 mm from the end, the stress initiated but did not produce a wave as shown in Figure 14.

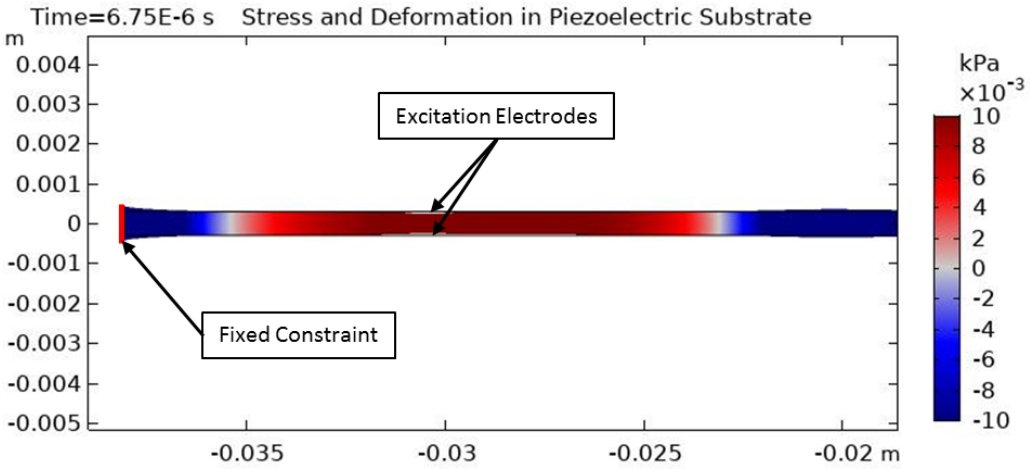

Figure 14 The x-direction stress and x-y deformation in the substrate with shifted electrodes when the acoustic wave starts to reflect off the fixed end. The deformation is increased by 7E6 times for visual purposes.

The reflection off the left end impacted the propagation and the wave was not allowed to reach the other end. The voltage excitation was changed from the sine wave to a Gaussian pulse, as seen in Figure 5. When the impulse is changed the material only expands once. The change makes it so the stress is just released as large deformation after the excitation ends. The stress and deformation for the Gaussian pulse is in Figure 15 below.

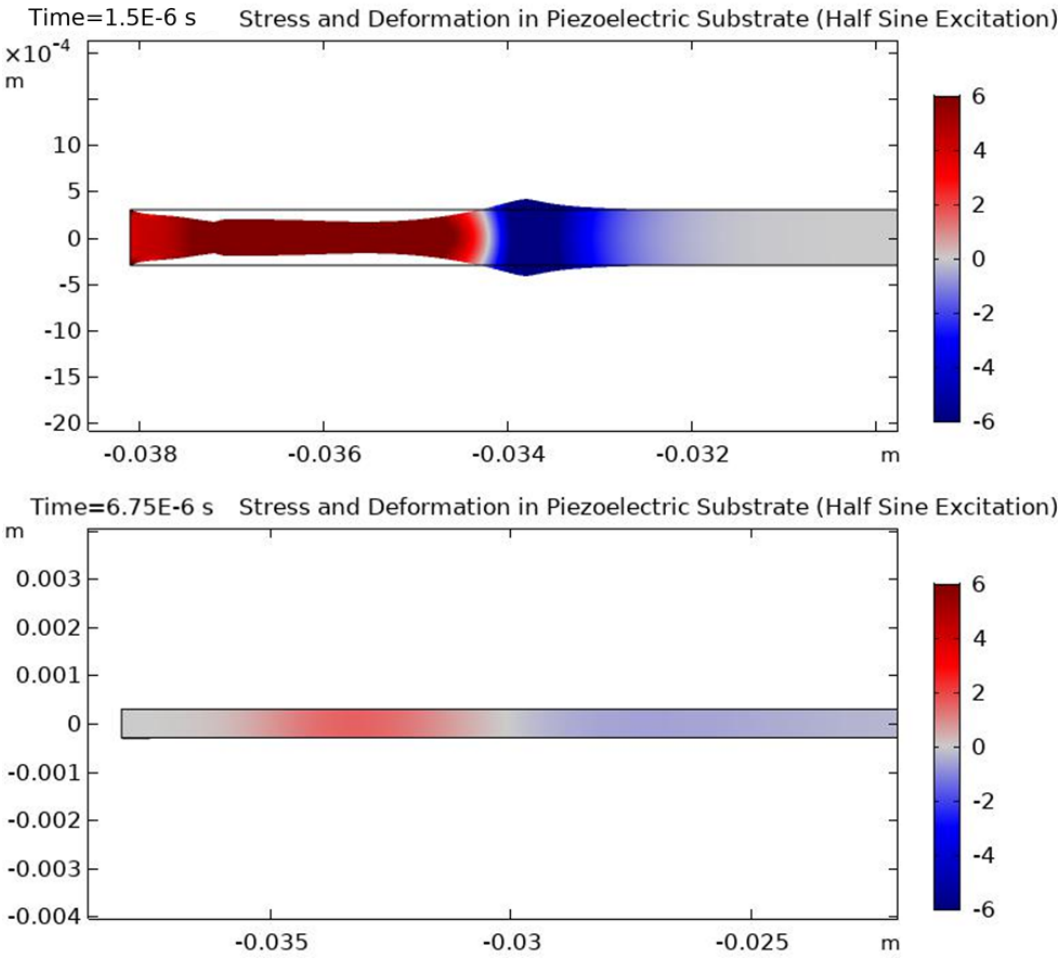

Figure 15 Comparison x-direction stress and x-y deformation in the substrate immediately after the end of the Gaussian pulse voltage excitation (top). And a short time after the excitation ends and stress is released (bottom). The deformation is increased by 7E6 times for visual purposes.

2.4 Conclusion

2.4.1 Vibrometer Testing

From the vibrometer testing the p-wave velocity was calculated as 2156.14±157.95 m/s at 95% confidence level. The nominal speed of the surface acoustic waves in lithium niobate is 3488 m/s. The error in the wave velocity can be related to the excitation used during the test. The substrate was impulse using the Nd:YAG laser. This excitation is at a single point. The propagation of the waves will be concentric to that

point. Since the laser excitation and the scanning field are aligned by hand this leaves for possibility of alignment error.

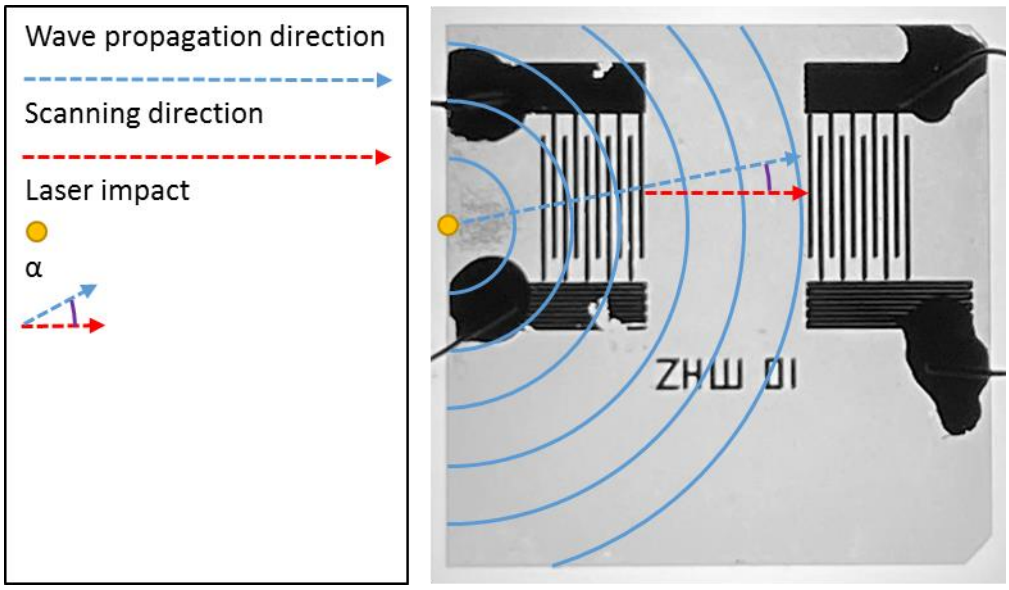

Figure 16 Possible wave propagation direction and the scanning field in lithium niobate substrate.

Figure 16 shows the possible alignment issue when testing. This difference could have caused the data to be less clear and have higher error. Exciting the material using electrodes and the piezoelectric effect will eliminate this error.

Since the substrate was not excited by the electrodes. This causes the waves to be misaligned with the sensing electrodes. The misalignment makes the electrode lead voltage in Figure 9 less significant and hard to interpret. The laser impulse caused the sensor to vibrate at resonance frequency instead of the 10 MHz the electrodes were designed to detect and generate. This mismatch also causes the electrodes to not read the correct voltage profile. There is still an electrical interference that occurs before the p-wave arrives through the material. To eliminate this interference, additional sensors will need to be tested where the sensing and excitation electrodes are on two separate pieces

of lithium niobate and attached to a passive and non-conductive material. Additional testing with the sensor impulsed using the electrodes will need to be done to allow for voltage excitation and sensing using electrode leads. The voltage excited sensor can be used to calculate a speed of sound. Then the speed of sound can be compared to new vibrometer data to determine sensor error.

2.4.2 Finite Element Analysis

2.4.2.1 Rayleigh SAW Sensor

As stress propagates through the sensor interactions and reflections occur at the boundaries of the substrate. These reflections interact with the shear waves by adding and subtracting, making the signal noise higher. The p-wave portion of the excitation is fastest and is not impacted by boundary reflections due to its speed. The p-wave is the first to arrive to the sensing electrode. Even though the p-wave is the first to arrive there is still a significant amount of electromagnetic field interference when the acoustic wave propagates in the piezoelectric material. This interference is why there is not a clear first arrival for the p-wave or shear waves when looking at the sensing voltage in Figure 11. The electromagnetic field interference has not been discussed or experimentally characterized in literature. Future experiments will need to be conducted to validate this observation. Another reason for not seeing a peak in voltage when the acoustic waves arrive is due to the small electric voltage that is induced from the piezoelectric effect. When looking at the stress in the model as it moves under the electrodes the stress amplitude changes in the area under each electrode. It is believed the electrodes act as a damper and absorbs some of the mechanical energy and reduces the electric potential created by the piezoelectric substrate.

2.4.2.2 Longitudinal-mode Sensor

During the simulation it was observed that the wave reflection on the left edge will interfere with the p-wave sensing. The electrodes were moved further into the substrate as shown in Figure 14. The resulting reflection in the left side of the substrate impacted the acoustic wave propagation. From this, no wave was detected from the sensing electrodes. This interaction could be solved by adding a damper to the left edge to completely eliminate the reflection. The shape of the impulse voltage also impacts the acoustic wave. When the model is excited by the Gaussian pulse, the material only expands once creating a single p-wave. This p-wave had a large wavelength and dispersed quickly as material expansion. Since the Gaussian pulse did not actuate at the same frequency as in the sine pulse, it is unknown whether the full sine wave is needed or just a higher frequency. Fine tuning the shape of the impulse voltage will help to maximize the p-wave output. When looking at the solid mechanics of the longitudinal-mode sensor model, the piezoelectric sensor produced p-waves regardless of the impulse or voltage profile. When the electrode is at the edge and the voltage profile is a sine pulse the stress in the material propagated through the substrate. The stress produced a voltage in the substrate from the piezoelectric effect. Once the wave reached the opposite end of the substrate the voltage was able to be transferred to the electrode. The plot of the voltage over time of the excitation and sensing electrodes are shown in Figure 13. Since the sensing electrode is at the end of the substrate then the wave starts to reflect back underneath the sensor immediately. The reflection is both constructive and destructive with the original wave. Additional models and testing will be needed to determine proper location of sensing electrode to properly find the wave amplitude.

CHAPTER THREE: MAGNETOSTRICTIVE ULTRASONIC THERMOMETER

3.1 Introduction

Magnetostrictive materials are another common form of actuation and sensing material. These materials convert energy between magnetic field and stress (bending, compression, or tension).

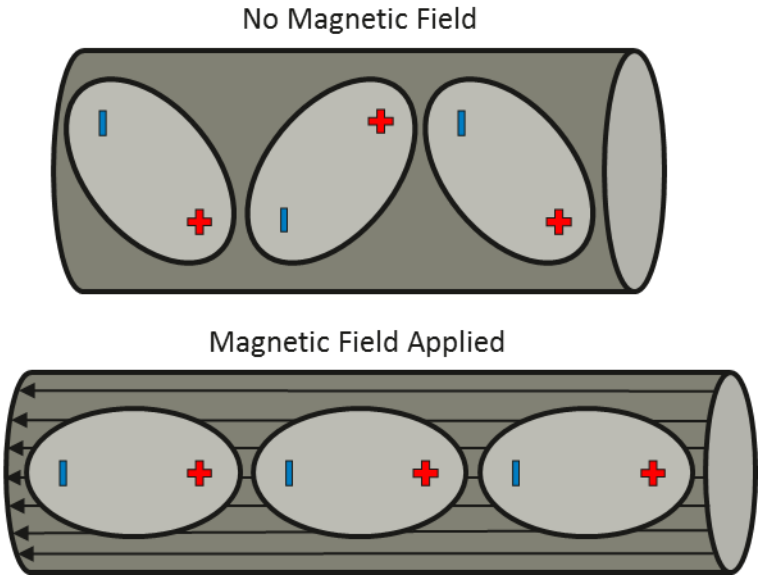

Figure 17 Magnetostrictive material before and after magnetic field is applied.

Magnetostrictive materials have a magnetic and mechanical linear relationship that is reliant on two dependent equations [8]. The first equation is the relationship between mechanical stress and strain and magnetic parameters:

$$\epsilon = \frac{\sigma}{E_y^H} + d\boldsymbol{H}, \qquad (3)$$

where ϵ is strain, σ is stress, E_y^H is Young's modulus at a constant applied magnetic field, $d = \partial\epsilon/\partial H|_\sigma$ is the strain magneto-mechanical coefficient, and H is the applied magnetic field [8]. The second equation is the magnetic induction equation:

$$\boldsymbol{B} = d^*\sigma + \mu^\sigma \boldsymbol{H}, \qquad (4)$$

where $d^* = \partial B/\partial\sigma|_H$ is the magnetomechanical coefficient, and μ^σ is the permeability at a constant stress [8]. As a magnetic field is applied to the magnetostrictive material the material strains. When an outside force acts on the material that causes it to strain, the magnetic field within the material will change. The back and forth coupled nature of this material allows for it to be used for both an actuation and sensing.

The method for finding temperature is similar to the piezoelectric materials outlined in chapter two. The major difference is magnetostrictive materials are actuated using coils and a magnetic field instead of a voltage applied to electrodes. This type of ultrasonic thermometer is being looked at by the INL for nuclear reactors due to its small size and ability to withstand high temperatures [2]. The small diameter wire also allows for dispersion of ultrasonic waves to be avoided [2]. INL tests have shown these sensors have increased accuracy when compared to other temperature sensing methods currently available [2].

Multiphysics FEA is needed to model the reflections seen during sensor testing. The model can help determine the speed of sound through the material and characterize the wave reflections. The modelling can also provide information on components that could improve the sensors. To ensure model accuracy, the model will be compared to data from the laser Doppler vibrometer and ultrasonic transducer experiments. Material

parameter tuning and system damping can be added to help tune the results to match FEA.

3.2 Methods

3.2.1 Testing

3.2.1.1 Magnetostrictive Transducer

The magnetostrictive ultrasonic thermometer consists of a galfenol wire inside a transducer with an AC driving coil and a DC bias coil. The galfenol in this case is used as a waveguide. The sensor dimensions and geometry are shown in Figure 18.

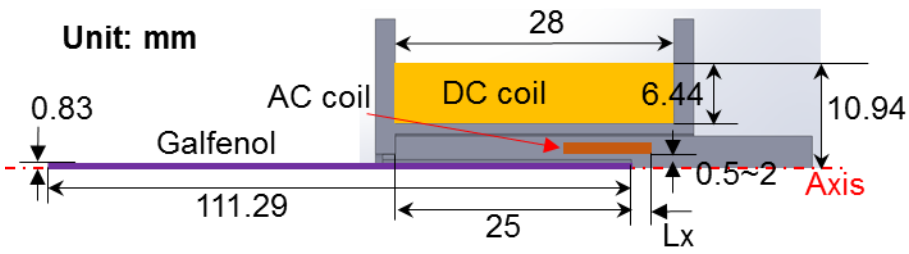

Figure 18 Dimensions and geometry of the cross section view of the magnetostrictive transducer and waveguide. The full sensor is revolved around center axis shown.

The galfenol used during testing is research-grade, 18.6% wt. gallium, 100-oriented, polycrystalline, and not stress-annealed. The AC coil is made of 200 turns in total with 50 turns in each layer of AWG 36 wire. The DC coil is made with 130 turns and AWG 18 wire. The casing around the AC coil is made of either SS-304 or SS-316. The AC coil was controlled by US Ultratek EUT3160 ultrasonic testing instrument. The EUT system is used as both the excitation and the sensor for this test. The impulse used was a 100V amplitude square wave with one half cycle.

Figure 19 Square wave with amplitude (A) and pulse width (W). Example of impulse voltage used for experiments pictured right.

Figure 19 shows the impulse voltage used by the EUT system for driving the coil. Half cycle is defined as half a sine wave. In Figure 19, the pulse on the left has three half cycles and the pulse on the right has one half cycle. The polarity in the EUT was set to negative, causing the square wave to start negative rather than positive, which is typically the case. The transducer frequency was set to be 200 kHz. The width of the pulse for the experiment is 2500 ns. The pulse width can be found by,

$$W = f^{-1}/2, \qquad (5)$$

where f is the transducer frequency. A gain of either 0 dB or 20 dB was used to increase the signal to noise ratio during testing. The DC bias current used was a constant 2 A. The EUT software has a built in signal filter with both low and high pass and were set to 9 MHz to 120 kHz respectively.

3.2.1.2 Vibrometer

Using the Polytec PSV-400 laser Doppler vibrometer a nickel wire was tested to directly measure the time of flight of the material. To eliminate any uncertainty of the acoustic wave excitation, a Nd:YAG laser was used to impulse the material rather than the magnetostrictive transducer. The vibrometer has a sampling frequency of 2 MHz and a minimum laser spot size of 36 μm and stacked each measurement 200 times to reduce noise in the signal. The entire end of the wire was impulsed at one end of the wire and the out of plane vibration was measured along a straight line on the side of the wire.

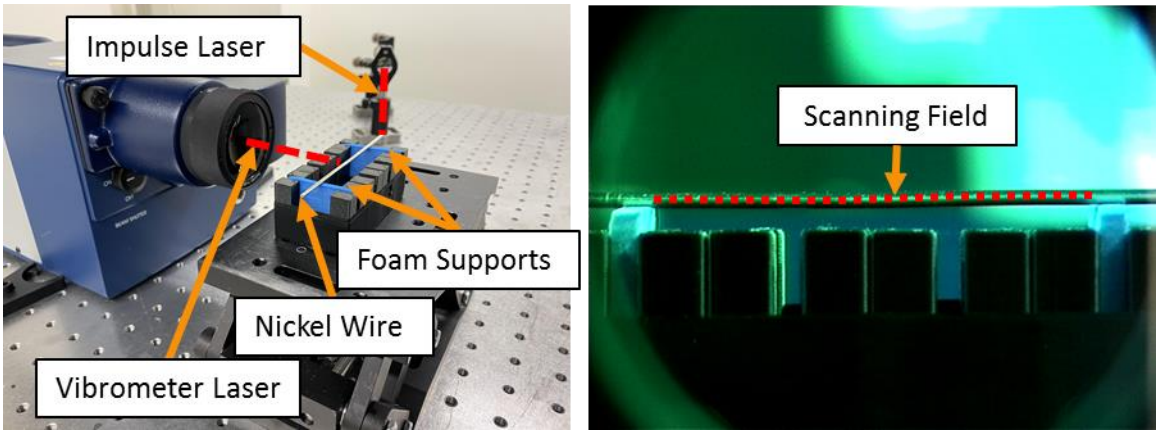

Figure 20 Nickel wire vibrometer experimental setup (left) and the scanning field used in testing (right).

The nickel wire is supported by two thin slices of foam to simulate a free-free boundary condition. The small contact area of the foam also keeps the energy loss to the foam low. The scanning field, shown in Figure 20, has a length of 50 mm with 130 data points evenly distributed.

3.2.2 Finite Element Analysis

A COMSOL Multiphysics FEA model was created to give insight into the wave propagation. Unlike analytical modeling, the FEA model can take into account the eddy current energy loss and more accurately model the speed of sound through the material. Due to its axisymmetric properties, the sensor can be modelled as a 2D axisymmetric model. The model consists of a galfenol wire inside a casing with an AC driving coil, as well as a DC bias coil that is all surrounded by an air domain. The model geometry is shown in Figure 21.

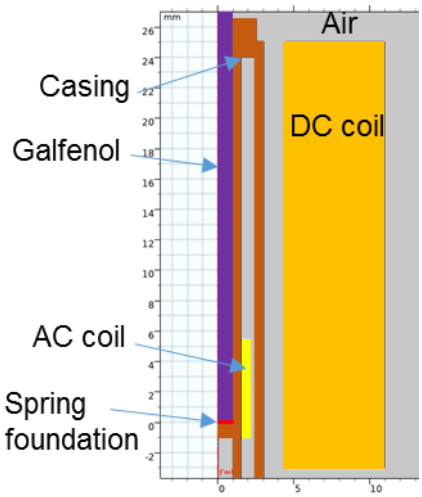

Figure 21 2-D axisymmetric model of galfenol waveguide sensor in COMSOL.

The magnetic dynamics is simulated for all components. The mechanical dynamics is only simulated in the galfenol wire. A spring foundation boundary condition with a spring constant of 1 N/m is used to restrict rigid body motion. In practice there is no spring and the galfenol wire is under free-free boundary conditions. The AC coil was impulse with the same square voltage pulse as the EUT system.

3.3 Results and Discussion

3.3.1 Testing

3.3.1.1 Magnetostrictive Transducer

To check the correct gain needed for the best signal-to-noise ratio a gain of 0 dB and 20 dB were used. The voltage measurement for both tests is shown in Figure 22.

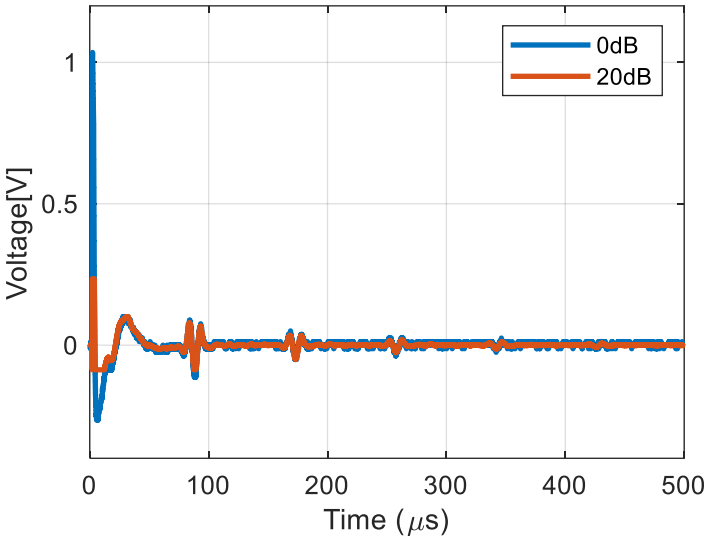

Figure 22 **Voltage comparison of 0 dB and 20 dB for DC current of 2 A and voltage Amplitude of 100 V.**

The measurements compared together shows the repeatability and that the 20 dB gain provides the best result and least noise. The signal also shows the high repeatability of the EUT ultrasonic testing instrument.

Using the data from the gain of 20 dB each reflections voltage amplitude, location, and time were collected and used to calculate a time of flight of the acoustic wave. A typical waveform was created to show where the data points were being taken from, shown in Figure 23.

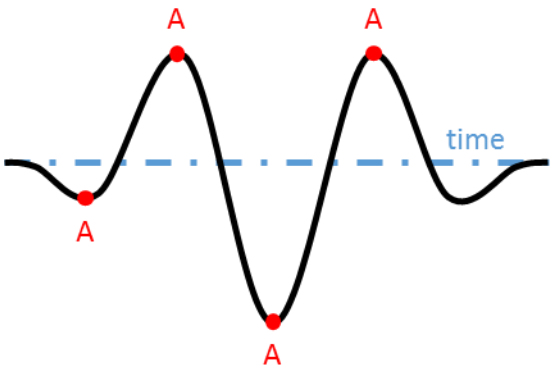

Figure 23 **A typical waveform of reflection voltage.**

The data points for each A_i were chosen manually with a time resolution of 0.05 μs. The summarized data taken from the 20 dB voltage profile is in Table 2.

Table 2 Reflection amplitudes and times for each location for galfenol waveguide.

Location	A_1		A_2		A_3		A_4	
	Time (μs)	Voltage (V)	Time (μs)	Voltage (V)	Time (μs)	Voltage (V)	Time (μs)	Voltage (V)
Reflection #1	79.3	-0.02586	83.9	0.07511	88.55	-0.112	93	0.06403
Reflection #2	163.2	-0.009851	168.3	0.03325	173.1	-0.05048	177.8	0.03201
Reflection #3	246.8	-0.003694	252.6	0.01478	257.6	-0.02586	262.6	0.01601
Reflection #4	330.8	-0.003694	336.4	0.006157	341.9	-0.01478	346.9	0.009851
Reflection #5	414.9	-0.002463	420.3	0.002463	425.8	-0.008619	431	0.004925

The amplitude of the voltage at point A_1 is smaller than the amplitude of the other points resulting in less reliability. The time of flight between each reflection was then determined and tabulated in Table 3.

Table 3 Calculated time of flight for galfenol waveguide between different reflections and locations.

Location	Reflection 1&2	Reflection 2&3	Reflection 3&4	Reflection 4&5
A_1	83.9	83.6	84.0	84.1
A_2	84.4	84.3	83.8	83.9
A_3	84.6	84.5	84.3	83.9
A_4	84.8	84.8	84.3	84.1

The time of flight is pretty consistent no matter which reflection is used, with the average time of flight of 84.13 μs. From the length of the rod and the average time of flight between reflections a wave velocity can be calculated. The average velocity of the wave is 2645.67 m/s.

3.3.1.2 Vibrometer

The out of plane vibration was collected for all the points along the scanning field. The data was then plotted as relative distance from the start of the scanning field and time, with vibration amplitude as the color. Then the data was filtered using a band pass filter to isolate the p-wave and the s-wave. Once isolated, the peaks of the wave were chosen and a linear regression found the best fit for each wave. The optimal fit lines as well as their corresponding velocities is shown in Figure 24.

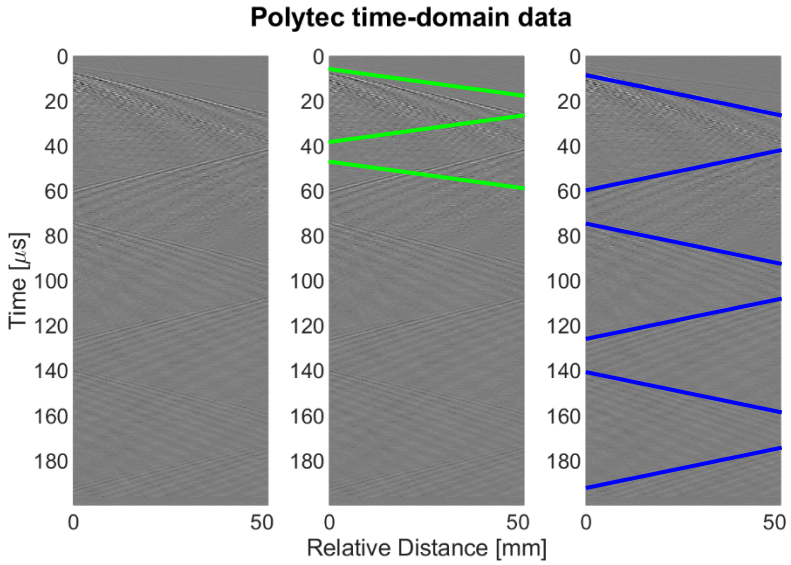

Figure 24 Vibration amplitude (color scale) over time along the scanning field of the nickel wire. Green line is the p-wave and the blue line is the s-wave.

The data also shows the multiple reflections that happen by each wave type by the single impulse. The velocity of the p-wave of the nickel is 4541.83±43.50 m/s at 95%

confidence level. The velocity of the s-wave is 2872.47±6.47 m/s at 95% confidence level.

3.3.2 Finite Element Analysis

Using the finite element model, the magnetic field due to the DC bias was checked when the current of the coil was at 2.0 A. The magnetic flux density of the galfenol material was used to check if the material is fully saturated. Figure 25 shows the resulting magnetic analysis.

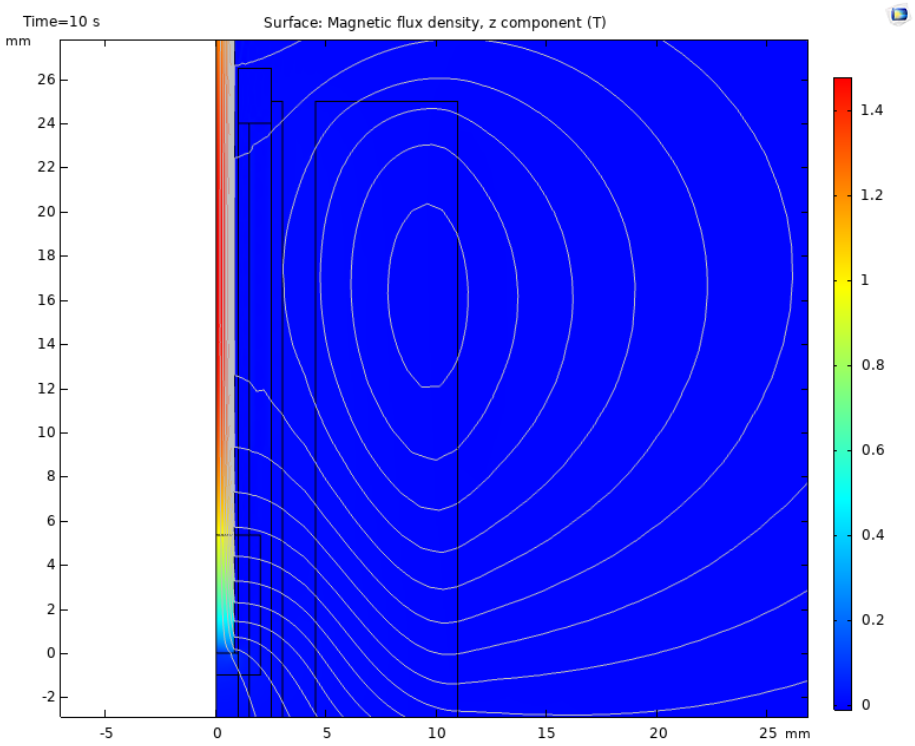

Figure 25 Magnetic flux density distribution when a current of 2.0 A is applied to the DC coil.

To measure the voltage output from the coil, the impulse needed to be converted from a voltage impulse to a current impulse. This was done by running a simulation first with the voltage impulse and plotting the resulting current. The resulting current is plotted in Figure 26.

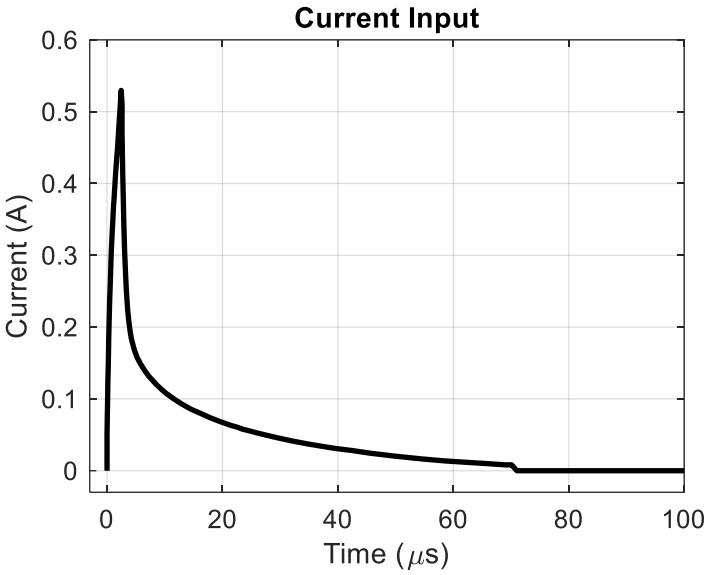

Figure 26 AC coil input current found using simulation.

After 70 μs the current had to be manually set to 0 A, because there was still significant oscillation. Figure 26 was then used as the input to the coil so that the voltage data could be read from the same coil domain. The voltage was then filtered using a band pass filter with band frequency from 120 kHz to 9 MHz. This filter is the same frequency used by the EUT system. The results were plotted along with the results measured from the EUT system for comparison.

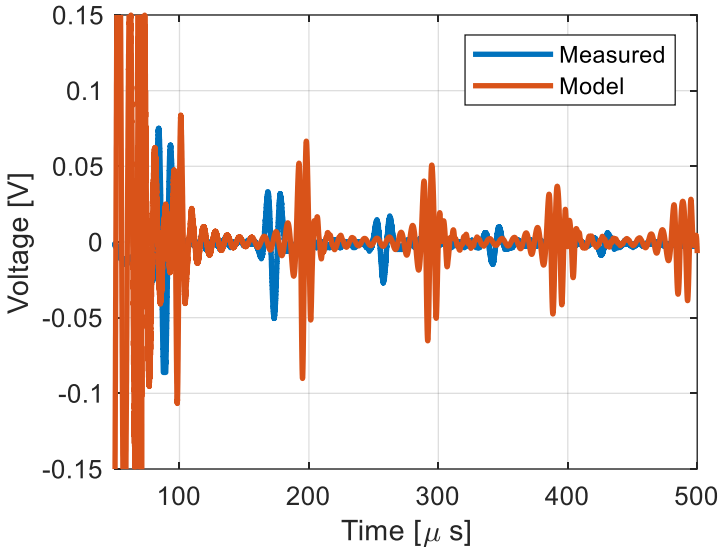

Figure 27 Comparison of simulated and measured voltage reflections.

The voltage amplitudes and times for the locations described in Figure 23 were obtained from the model voltage data. The data is summarized in Table 4.

Table 4 Voltage amplitude and time data for reflection locations from COMSOL simulation.

Location	A_1		A_2		A_3		A_4	
	Time (µs)	Voltage (V)	Time (µs)	Voltage (V)	Time (µs)	Voltage (V)	Time (µs)	Voltage (V)
Reflection #1	92.7	-0.01991	95.85	0.04769	98.35	-0.1067	101	0.0836
Reflection #2	188.4	-0.02251	192.3	0.05209	195.1	-0.09017	198	0.06666
Reflection #3	284.8	-0.01858	288.9	0.04029	291.8	-0.06531	294.9	0.05085
Reflection #4	381.3	-0.01526	385.6	0.03159	388.5	-0.04758	391.9	0.03685
Reflection #5	477.8	-0.01234	482.1	0.02465	485.2	-0.0345	488.8	0.0269

The time of flight for the model results were calculated using the data in Table 4. The summary of time of flights for the simulated reflection data is tabulated for each location and between each reflection.

Table 5 Calculated time of flight for galfenol waveguide between different reflections and locations from COMSOL simulation.

Location	Reflection 1&2	Reflection 2&3	Reflection 3&4	Reflection 4&5
A_1	95.7	96.4	96.5	96.5
A_2	96.45	96.6	96.7	96.5
A_3	96.75	96.7	96.7	96.7
A_4	97	96.9	97	96.9

The data from Table 5 resulted in an average time of flight of 96.68 μs. When compared to the results from the experiment the simulation time of flight was 12.53% higher. The average wave velocity for the simulation was calculated as 2302.23 μs.

3.4 Conclusion

The time of flight for the EUT system measurements gradually increases as the wave propagates, this is from the slight variation in galfenol. This variation comes from the changing Young's modulus in the magnetostrictive material due to the Delta-E effect [9]. The Young's modulus of galfenol (research grade and 18.6% wt. Gallium) varies between 45 GPa to 71.9 GPa, when it is biased by a solenoid [9]. This leads to a large variation in speed of sound through the material. TdVib LLC has the speed of sound for research grade galfenol ranging from 2265-2775 m/s. The speed of sound is likely the s-wave of the material rather than the p-wave due to its lower velocity. To test this, a combination of the EUT transducer excitation as well as the laser Doppler vibrometer can

be used. This test will allow for a direct measurement of the excitation waves and speeds and be able to characterize the error present using the EUT system. The vibrometer testing verified the experimental setup that can be used to obtain velocities for the galfenol wires. The nickel wire velocity for the p-wave of the nickel is 4541.83±43.50 m/s and the s-wave is 2872.47±6.47 m/s at 95% confidence level. Since nickel is a common material, the p-wave and s-wave velocity can be found in most material databases. The Engineering ToolBox has the p-wave velocity as 4900 m/s and the s-wave velocity as 3000 m/s. The percent difference in the nickel p-wave and s-wave velocity is 7.31% and 4.25% respectively. The small difference in the known to the measured could be due to possible imperfections in the material and its shape. The imperfections could slightly change the reflections and the speed of sound through the material.

CHAPTER FOUR: CAPACITANCE BASED STRAIN GUAGE

4.1 Introduction

Flexible capacitance based strain gauges can be used for evaluation on any soft structural material. The strain sensor is non-destructive and can be used for structural health monitoring to ensure safety. It can monitor the strain and load in real time and provide the ability to locate damage and diagnose issues [6]. Boise States ANML manufactured a CSG and tested the sensor.

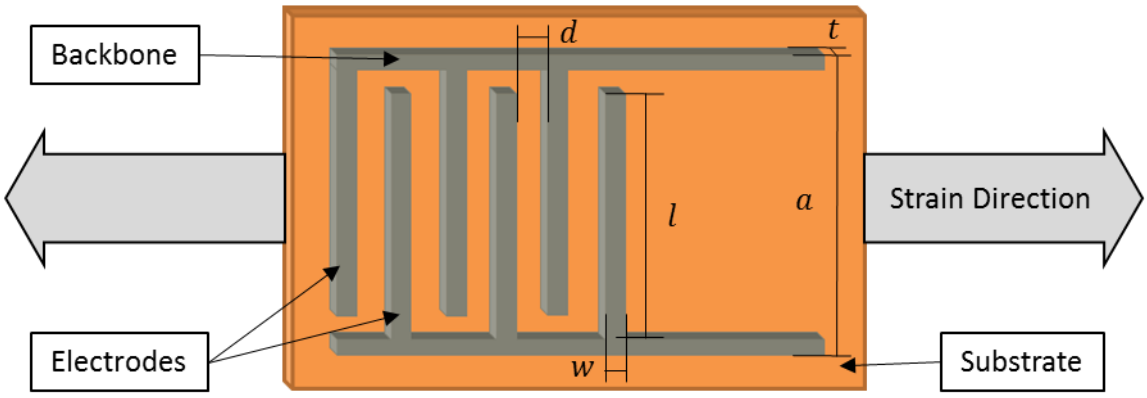

Figure 28 Diagram of CSG layout and design that is similar to the manufactured and tested sensor. Dimension variables shown are used in the capacitance equations (6) and (7).

Figure 28 shows a sensor similar to the one manufactured by ANML. The key difference between Figure 28 and the manufactured sensor is the number of electrodes in each pair. The actual sensor consists of two sets of 50 electrodes that are connected by the backbone. There are two equations that govern the capacitance of the sensor. The first equation is the initial unstrained capacitance:

$$C_0 = pt(2l - a + 2w)\left(\frac{2n-1}{d}\right)\varepsilon_0, \qquad (6)$$

where C_0 is the initial capacitance, p is the dielectric constant of the PMMA that is over the electrodes, t is the thickness of the silver electrode, l is the length of the electrode, a is the width of the interdigital electrode pair, w is the width of the silver electrode, n is the number of digit pairs of electrodes, d is the spacing between the electrodes, and ε_0 is the permittivity of the free space [6]. The second equation is the strained capacitance:

$$C_{xN} = pt(2l - a + 2w)\left(\frac{2n-1}{d+x}\right)\varepsilon_0, \qquad (7)$$

where x is the deformation in the sensitive axis. The sensor works by increasing the distance between the electrodes causing a decrease in capacitance [6].

When the material was tested, the unstrained capacitance measured 42 pF and when the material was strained to 10% the capacitance was 15 nF [6]. The analytical equations above were used to compare the measured values. The initial unstrained capacitance from the analytical equation was found to be 2.44 pF [6]. The analytical equations are limited to one direction of sensitivity, when in practice the shape change due to strain also impacts the capacitance. The equations also assume bulk materials, under a scanning electron microscope the silver electrodes were porous [6].

A FEA model was created to explore the reasoning behind the difference between the analytical equation and the actual measurements. The model allows for multidirectional strains to be considered. The model assumes bulk materials, allowing for the interaction between multidirectional strain and material porosity to be analyzed. The model can help determine which of these factors cause the difference.

4.2 Methods

Modeling using multiphysics can be used to verify interdependencies of theory and physical testing. COMSOL Multiphysics can allow for strain (solid mechanics) to be solved at the same time as capacitance (electrostatics).

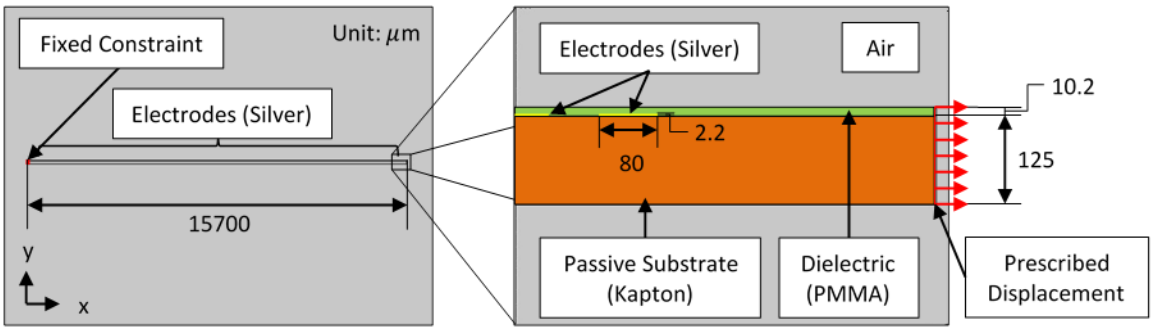

Figure 29 Capacitive sensor model geometry and boundary conditions.

Figure 29 is a 2-D cross sectional view model constructed in COMSOL Multiphysics. The thickness of this model (depth along the out of plane z-axis) is 15.1 mm. A circular air domain with a radius of 23.55 mm is defined to replicate the infinite air around the sensor in practice. The strain gauge is fixed on the left end. A boundary displacement is prescribed along the x-axis on the other end of the sensor, as shown in Figure 29. The displacement is increasing at a constant rate of 0.1 mm/s. A total of 100 silver electrodes are evenly distributed along the x-axis on the substrate. Each electrode is represented by an 80 by 2.2 micron rectangular domain. To detect the capacitance, every other electrode had to be linked, one set was for the constant voltage of 1 V, and the other set was for the ground and had no electrical charges. The capacitance between two sets of electrodes are calculated by the lumped parameters using the energy method. Material porosity is ignored and material properties used in this study are summarized in Table 6.

Table 6 Key material properties used in the physics of the COMSOL model

Material	Young's modulus (GPa)	Density (kg/m^3)	Poisson's ratio	Relative permittivity
Silver	83	10500	0.37	100000
Kapton	2.8	1420	0.34	4
PMMA	3	1190	0.4	4.9
Air	–	–	–	1

4.3 Results and Discussion

The input displacement strains the substrate and changes the spacing between electrodes. Therefore, the capacitance varies with respect to the prescribed displacement.

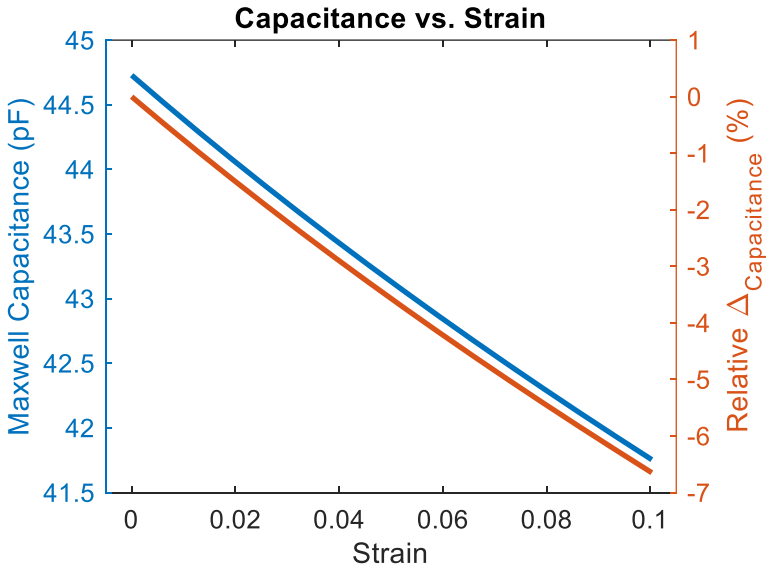

Figure 30 Maxwell capacitance and relative change in capacitance with increase in strain.

Figure 30 shows that the capacitance decreases from 44.73 pF to 41.75 pF as the substrate strain increases from 0 to 10%. This corresponds to a gauge factor of 0.663. A sensitivity study of the electrode parameters was done to determine the best parameters

for the CSG. The sensitivity is displayed using the gauge factor for the capacitance. The gauge factor for the different electrode height and width is shown in Figure 31.

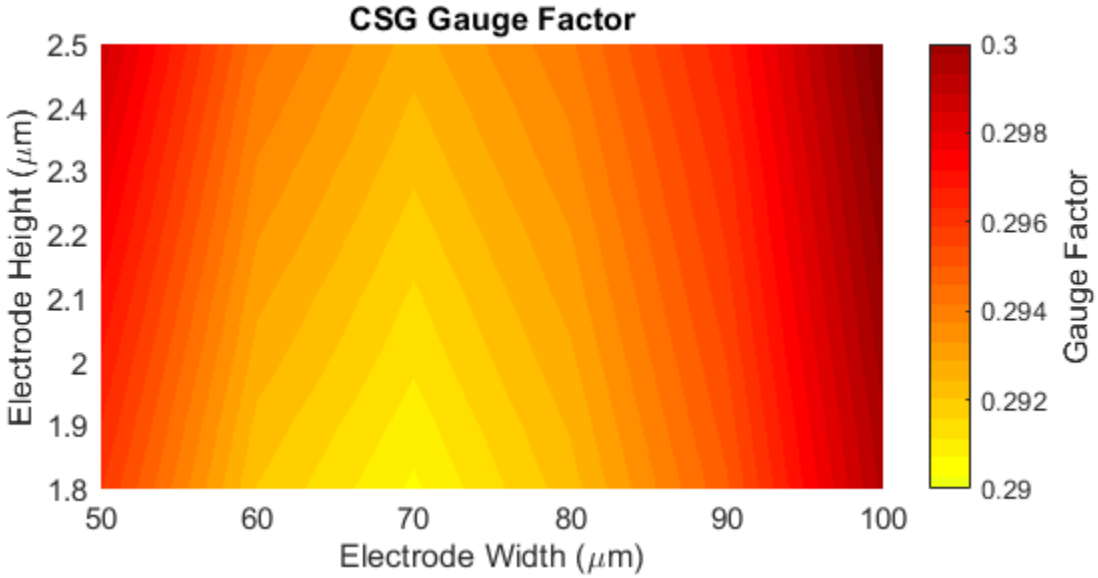

Figure 31 Gauge factor for changing electrode height and width.

4.4 Conclusion

The FEA model was able to better predict the initial unstrained capacitance, but was unable to get the same strained capacitance. The silver electrodes in the CSG are porous and are not completely uniform due to the manufacturing techniques used. This porosity is thought to be the reason for the large difference between the analytical model and the FEA model to the actual measured capacitance. Attempts were made to recreate the porosity inside the model but the model is incapable of modeling a large scale deformation and strain problem along with the microscale pores the material possesses. The sensitivity study did not result in a large variation in sensitivity as the parameters were changed. The gauge factor for modeling is limited due to the strained voltage not matching the actual sensor measurements. Continued model development will help to improve accuracy and produce better guidance for future designs.

CHAPTER FIVE: LINEAR VARIABLE DIFFERENTIAL TRANSFORMER

5.1 Introduction

Linear variable differential transformers are a common linear displacement sensor. It converts linear mechanical displacement into an electrical signal that can then be used to find a numerical value for displacement. This sensor has “infinite” resolution that is only limited by the sensors noise. The LVDT consists of an excitation coil and two sensing coils that surround a magnetic core. A generalized LVDT sensor is shown in Figure 32.

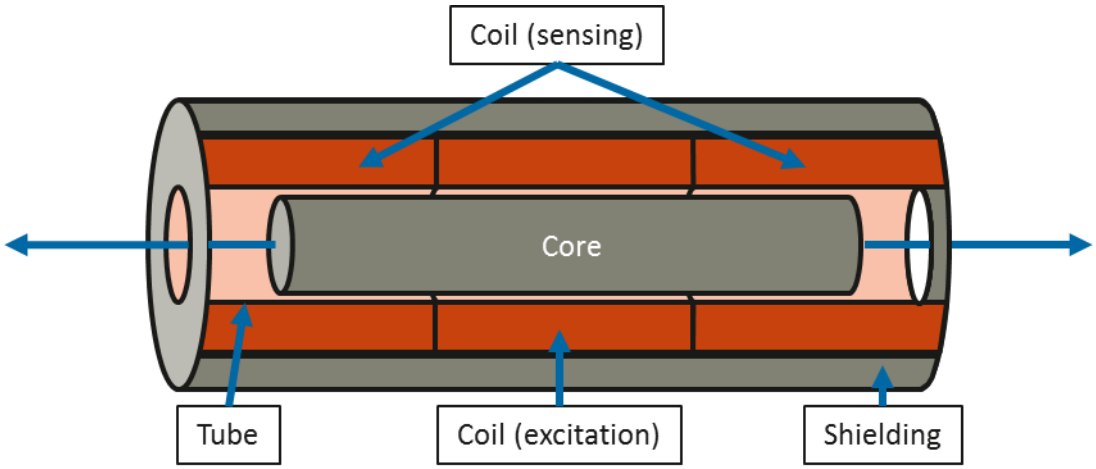

Figure 32 General LVDT component diagram.

The device uses the magnetic field produced by the excitation coil and the core then measures the voltage in each coil and the difference is computed. The equations and a diagram on the basics of how the LVDT works is shown in Figure 33.

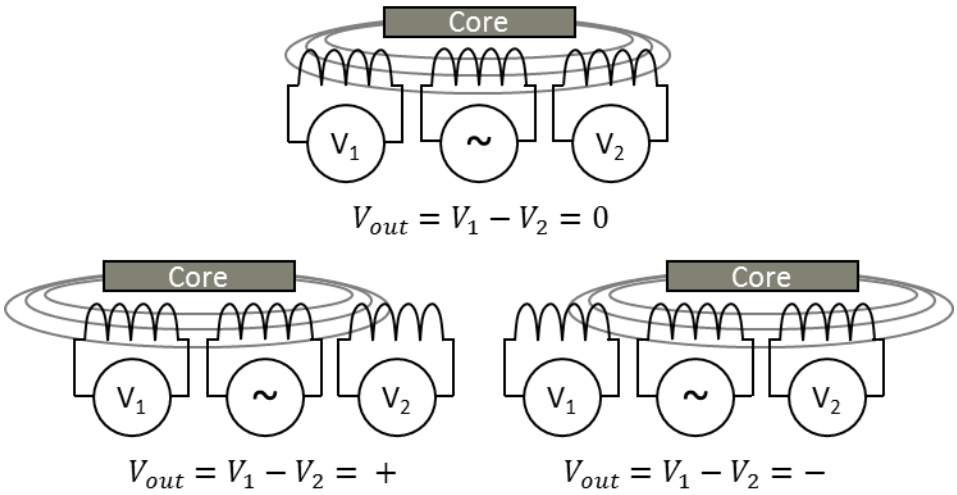

Figure 33 Equation and basic operation diagram of LVDT sensor.

Output voltage (V_{out}) can then be related to known displacements and a characterization equation can be developed to convert the output voltage into displacement.

Monitoring of irradiation of new materials for use in new and existing reactors to test for dimensional changes was previously done post removal [10]. The post removal process was expensive and time consuming. The Halden Reactor Project have used the LVDT sensors to detect mechanical changes and is the base sensor used in detecting fuel elongation, cladding elongation, fuel centerline temperature, and fuel rod pressure [5]. The INL used commercial LVDT devices to provide live, inexpensive data [10]. The commercial LVDT sensors have temperature and material limitations along with design size [10]. A high temperature and miniaturized sensor needs to be developed to address the short comings of the commercial sensors. An exploration into adding a fiber optic cable through the core is also needed to evaluate the effects without damaging existing sensors. Multiphysics FEA was used to help provide data on sensor miniaturization and adding fiber optic cables. The FEA will be tuned using the characterization data that was provided by the INL.

5.2 Methods

The INL tested an LVDT device and got characterization data for the core displacement. The displacement in the core and the voltage output is plotted in Figure 34. The data was tested at 7V RMS and at a frequency of 5 kHz. The device sensitivity is 6.53 mV/V/mm.

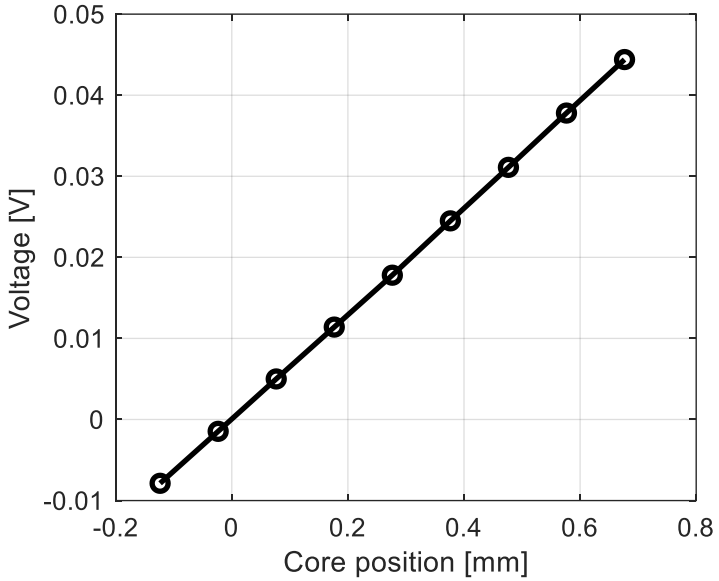

Figure 34 LVDT characterization data measured at the INL.

Using the axisymmetric property of the LVDT system, a 2-D axisymmetric FEA model was created using COMSOL Multiphysics. The model consists of two sensing coils, one driving coil, a magnetic core, tubing, and shielding that are all surrounded by an air domain. The model geometry is shown in Figure 35.

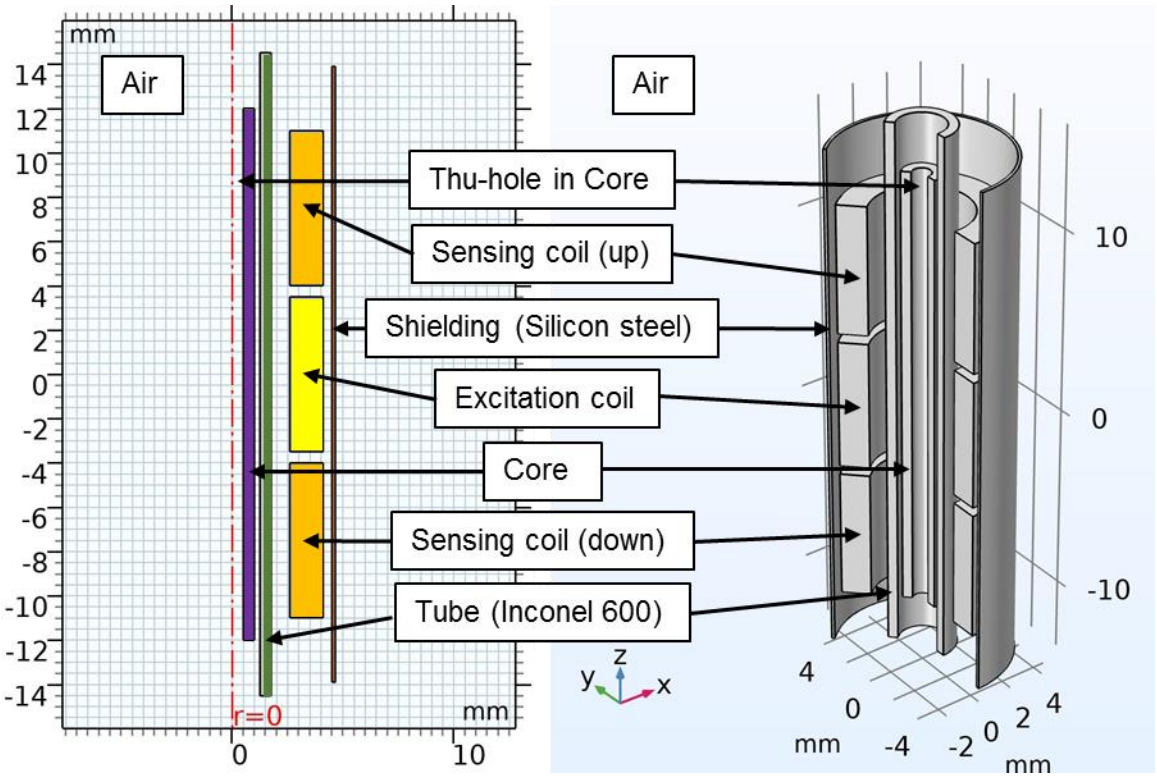

Figure 35 2-D axisymmetric model of the LVDT sensor.

The model also includes a thru-hole in the core that ranges in size from no hole to 0.75 mm. The LVDT is surrounded by a circular air domain with a radius of 100 mm. All the coils are simulated as homogenized multi-turn coil domains with AWG 36 wire. The thru-hole study is to characterize the impact of drilling a hole in the core to place optical fibers through in practice. The excitation voltage for the model is a sinusoidal wave with an amplitude of 1 V and a frequency of 1 kHz. Both a time-domain analysis and a frequency-domain analysis was studied. The time-domain analysis was done at steady state. The voltage output is calculated from the amplitude of the difference in voltage across the sensing coil (up) and the sensing coil (down). The estimated number of turns is 430. Two approaches to the model were done, the first approach assumed a linear core permeability and the second approach the measured nonlinear permeability was used. The nonlinear magnetic permeability used for the model was shown in Figure 36.

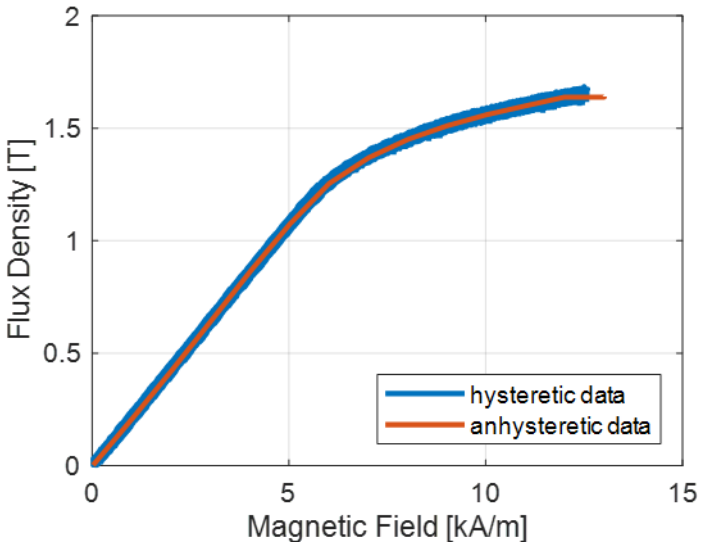

Figure 36 Nonlinear HB curve for LVDT core.

The core is assumed to be linear when the magnetic field is below 5 kA/m and the magnetic flux density is below 1.1 Tesla. Linear regression calculated the linearized magnetic permeability as 232.5. The sensitivity is calculated for each solution method and is calculated using the following equation:

$$S = \frac{sign(P)|V_{out}|}{|P||V_{ex}|}, \qquad (8)$$

Where P is the core position, V_{out} is the output voltage, and V_{ex} is the excitation voltage. The symbol "||" represents the amplitude of the signal. To test the impact a hole in the LVDT core has on the sensor a sensitivity study was done. The simulation was a linear magnetic permeability frequency-domain analysis with a fixed core position of 1 mm.

5.3 Results and Discussion

When the permeability is assumed to be linear the model for both time-domain and frequency domain yield the similar results. The difference in frequency-domain sensitivity was 4.3% smaller than the non-linear permeability with time-domain results. Since the difference in sensitivity was low, linear permeability was assumed for the rest

of the models. The frequency and time-domain analysis with linear permeability produced the exact same sensitivity. The frequency-domain analysis reduced the computation time by 87% when compared to the time-domain analysis. Due to having no difference in sensitivity and large reduction in computation time, the frequency-domain study was used for the rest of modeling. The sensitivity of the sensor is 4.21 mV/V/mm. The voltage output for the sensor for the frequency-domain is shown in Figure 37.

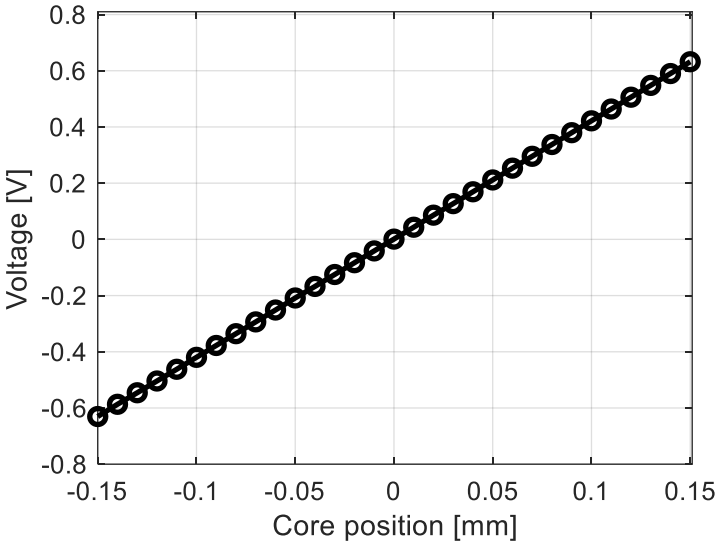

Figure 37 Voltage output of LVDT relative to the core position for frequency-domain.

Since both of the types of simulations produced the same result, the computation time was looked at to determine the best solution method.

The sensitivity of the sensor when a thru-hole is introduced to the core acts as expected. The sensitivity decreases as the hole radius gets closer to the 1 mm radius of the core. The sensitivity to the hole radius is in Figure 38.

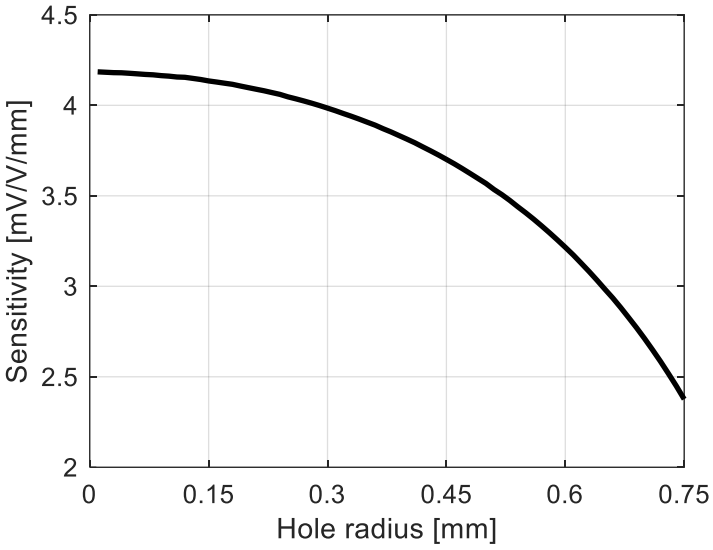

Figure 38 Sensitivity for an added thru hole in the core of the LVDT sensor.

5.4 Conclusion

The sensor sensitivity is highly reliant on the voltage amplitude and driving frequency. At steady state conditions for 1 V and 1 kHz the sensor has a sensitivity of 4.21 mV/V/mm. The percent difference between the model and the device is 35.5%. The difference is likely due to the difference in driving frequency between the model and the experimental data. A thru-hole in the core only decreases sensitivity. If maximum sensitivity is to be maintained and a fiber optic cable is to be added, the thru-hole should be as small as possible. Once better information on the INL data is collected, the model can be better compared to the experimental data. Fine tuning of model parameters can be done to help improve model accuracy to the experimental data.

CHAPTER SIX: CONCLUSIONS

Using FEA and experimental testing all the sensors can have improved development. The ultrasonic sensors both have good models, but will need fine tuning to provide verification. The fine tuning will be done through data obtained using the laser Doppler vibrometer and the EUT system. The setup for the experiments described in this thesis can be used, but future testing of the device will need to be done to get data that can be used for model verification. The first test is the galfenol wire with the EUT system and the laser Doppler vibrometer. The combination of those two tests will help tune the material properties in the model and improve model accuracy. The test for lithium niobate will be similar. The EUT system will be used to excite the material using the electrodes, then the vibrometer will be used along with the sensing electrodes to determine speed of sound. The CSG will need to try and provide a better more accurate model. Exploration in a 3-D model could help produce better accuracy. The 3-D model will not assume plane strain and could produce the higher resolution and gauge factor shown in experiments. Once a verified model is done more parametric studies can be done to show how the physical parameters change the sensor resolution. The LVDT model needs to be verified at the correct frequency. Once the verification is complete then parametric sweeps of parameters can be done for this device. These studies will be aimed for high resolution miniaturized devices. The development of these models has led to experience in FEA, experimentation, and project management.

This project is a great culmination of all my engineering skills and knowledge. Balancing four different devices for testing and modelling was challenging. The challenges helped me develop my professional skills in time management and prioritization. Each device had their own set of requirements that needed to be met according to the INL schedule, with monthly, quarterly, and yearly updates and deliverables. My knowledge of engineering has greatly broadened directly due to these sensors. I have increased knowledge in electrical engineering, material science, and geoscience. This will allow me to better communicate with people in other teams and be a more valuable team member in future jobs. The research taught me a lot about self-learning. Although I am done with my formal education the skills I obtained will help me continue my learning.

REFERENCES

[1] “Almost All U.S. Nuclear Plants Require Life Extension Past 60 Years to Operate beyond 2050.” U.S Energy Information Administration, www.eia.gov/todayinenergy/detail.php?id=19091.

[2] Daw, J., et al. “NEET In-Pile Ultrasonic Sensor Enablement-Final Report.” No. INL/EXT-14-32505. Idaho National Laboratory (INL), 2014.

[3] M. E. Morales-Rodríguez, P. C. Joshi, J. R. Humphries, P. L. Fuhr and T. J. Mcintyre, "Fabrication of Low Cost Surface Acoustic Wave Sensors Using Direct Printing by Aerosol Inkjet," in IEEE Access, vol. 6, pp. 20907-20915, 2018.

[4] Knudson, D. L., and J. L. Rempe. "Linear variable differential transformer (LVDT)-based elongation measurements in Advanced Test Reactor high temperature irradiation testing." Measurement Science and Technology 23, no. 2 (2012): 025604.

[5] S. Solstad, R. Van Nieuwenhove, “Instrument capabilities and developments at the Halden reactor project”, Nuclear Technology, 173(2011) 78-85.

[6] Kiyo T. Fujimoto, J. Watkins, T. Phero, K. Tsai, D. Litteken, B. Jaques, D. Estrada, “Aerosol Jet Printed Capacitive Strain Gauge for Soft Structural Materials”, Nature Partner Journals Flexible Electronics. (In Review)

[7] Weis, R. S., and T. K. Gaylord. "Lithium niobate: summary of physical properties and crystal structure." Applied Physics A 37, no. 4 (1985): 191-203.

[8] Calkins, Frederick T., Alison B. Flatau, and Marcelo J. Dapino. “Overview of Magnetostrictive Sensor Technology.” Journal of Intelligent Material Systems and Structures 18, no. 10 (October 2007): 1057–66. doi:10.1177/1045389X06072358.

[9] Deng, Zhangxian, et al. "Quasi-static major and minor strain-stress loops in textured polycrystalline Fe81. 6Ga18. 4 Galfenol." Journal of Applied Physics 120.24 (2016): 243901.

[10] D. Knudson, J. Rempe, J. Daw, “Evaluation of Candidate Linear Variable Displacement Transducers for High Temperature Irradiations in the Advanced Test Reactor”, Idaho National Laboratory (INL), 2009.